

Presynaptic protein synthesis is required for long-term plasticity of GABA release

Thomas J. Younts^{1, 4, 6, *}, Hannah R. Monday^{1, 4}, Barna Dudok^{3, 4, 5}, Mathew E. Klein^{1, 5},
Bryen A. Jordan^{1, 2}, István Katona³, and Pablo E. Castillo^{1, 7*}

¹Dominick P. Purpura Department of Neuroscience,

²Department of Psychiatry and Behavioral Sciences

Albert Einstein College of Medicine, New York, USA

³Momentum Laboratory of Molecular Neurobiology, Institute of Experimental Medicine, Hungarian Academy of Sciences, Budapest, Hungary

⁴School of Ph.D. Studies, Semmelweis University, Budapest, Hungary

⁴Co-first author

⁵Equal Contribution

⁷Lead Contact

*Correspondence:

Pablo E. Castillo, M.D., Ph.D.
Dominick P. Purpura Department of
Neuroscience
Albert Einstein College of Medicine
Rose F. Kennedy Center, Room 703
1410 Pelham Parkway South
Bronx, NY 10461, USA
Phone: +1.718.430.3262
E-mail: pablo.castillo@einstein.yu.edu

Thomas J. Younts, Ph.D.
⁶Present Address:
Department of Neuroscience, Physiology and
Pharmacology
University College London
Gower Street
London WC1E 6BT, UK
Phone: +44.020.7679.3214
E-mail: t.younts@ucl.ac.uk

Number of:

Pages: 32

Figures: 7

Supplementary Figures: 7

Total number of words:

Summary: 150; Introduction: 616; Experimental Procedures: 444;

Results: 2,819; Discussion: 1,409

Total character count in this entire document (including spaces): 71.810

Author Contributions: TJY, MEK, and PEC conceived and TJY and PEC directed the project. TJY, HRM and MEK performed electrophysiology and analyzed data; TJY performed cell paired recordings and two-photon microscopy; HRM performed second-harmonic generation microscopy; MEK performed PCR; HRM and BAJ performed FUNCAT; BD and IK performed STORM microscopy and analyzed data. TJY and PEC wrote and all authors reviewed and edited the manuscript.

Acknowledgements: We thank all Castillo lab members for discussions, Stefano Lutz and Pablo Lituma for technical assistance with field recordings and two-photon laser imaging, and Carlton Christie for field recordings; Balázs Pintér and Erika Tischler for technical assistance, and Kata Kenesei, Máté Kisfali and Benjamin Barti for slices. We acknowledge Vera DesMarais and David Entenberg at the Einstein Analytical Imaging Facility for help with second harmonic generation microscopy; and László Barna, the Nikon Microscopy Center at the Institute of Experimental Medicine, Nikon Europe B.V., Nikon Austria GmbH, and Auro-Science Consulting Kft for providing STORM microscopy support. We also thank Masahiko Watanabe for antibodies. Supported by the National Institutes of Health (R01-MH081935 and R01-DA17392) to PEC; (R01-NIAAG039521) to BAJ; and (F31-NS073200 and T32-GM007288) to MEK; European Research Council (Grant 243153), Momentum Program (LP2013-54/2013), and Wellcome Trust International Senior Research Fellowship (090946/Z/09/Z) to IK; and in later stages, The Royal Society (Newton International Fellowship) to TJY. There are no conflicts of interest.

Summary

Long-term changes of neurotransmitter release are critical for proper brain function. However, the molecular mechanisms underlying these changes are poorly understood. While protein synthesis is crucial for the consolidation of postsynaptic plasticity, whether and how protein synthesis regulates presynaptic plasticity in the mature mammalian brain remains unclear. Here, using paired whole-cell recordings in rodent hippocampal slices, we report that presynaptic protein synthesis is required for long-term, but not short-term, plasticity of GABA release from type-1 cannabinoid receptor (CB₁)-expressing axons. This long-term depression of inhibitory transmission (iLTD) involves cap-dependent protein synthesis in presynaptic interneuron axons but not somata. Translation is required during the induction, but not maintenance, of iLTD. Mechanistically, CB₁ activation enhances protein synthesis via the mTOR pathway. Furthermore, using super-resolution STORM microscopy, we revealed eukaryotic ribosomes in CB₁-expressing axon terminals. These findings suggest that presynaptic local protein synthesis controls neurotransmitter release during long-term plasticity in the mature mammalian brain.

Highlights

- Presynaptic protein synthesis is required for long-term depression of GABA release
- iLTD involves cap-dependent translation in interneuron axons but not somata
- CB₁ activation enhances protein translation via mTOR signaling
- Eukaryotic ribosomes are present in inhibitory interneuron axons and terminals

eTOC Blurb

The role of presynaptic translation in long-term plasticity in the mature mammalian brain is controversial. Younts *et al.* find that presynaptic protein synthesis is essential for long-term plasticity of GABA release at rodent hippocampal inhibitory synapses.

Introduction

Long-term plasticity of neurotransmitter release critically regulates circuit function (Castillo, 2012). Despite decades of research, the molecular basis of long-term changes in neurotransmitter release remains unsolved. While synthesis of new protein is required for stabilizing synapses during postsynaptically-expressed forms of long-term plasticity (e.g. long-term potentiation; LTP and long-term depression; LTD) (Buffington et al., 2014; Santini et al., 2014), whether and how presynaptic protein synthesis is involved in long-term presynaptic plasticity in the mature mammalian brain is unclear. Resolving this issue is important because LTP and LTD are linked to cognition, and dysregulated translation during long-term plasticity is associated with autism, Fragile X Syndrome, and Alzheimer Disease (Buffington et al., 2014; Darnell and Klann, 2013; Santini et al., 2014).

Presynaptic local protein synthesis, a process whereby mRNAs are translated in axons and terminals, can endow remote neuronal compartments with the flexibility to rapidly respond to local synaptic activity, independent of the soma (Alvarez et al., 2000). Although ribosomes have routinely been documented in mammalian axonal growth cones during early embryonic development, as well as in regenerating, cultured, and peripheral sensory axons (for recent reviews, see Crispino et al., 2014; Gomes et al., 2014; Holt and Schuman, 2013; Jung et al., 2014), the prevailing view is that fully developed axons in the healthy mammalian brain are incapable of supporting protein synthesis. In non-mammalian preparations, where translation inhibitors can be injected into relatively large axons, a role for local protein synthesis during long-term plasticity has been established (Beaumont et al., 2001; Martin et al., 1997; Zhang and Poo, 2002). Mammalian central nervous system (CNS) axons are considerably smaller and therefore, more difficult to experimentally manipulate. To date, a direct demonstration for a

requirement for presynaptic protein synthesis during long-term plasticity in an intact mammalian CNS circuit is lacking. Moreover, there is very little evidence for the presence of ribosomes inside fully developed presynaptic axon terminals.

One of the most ubiquitously expressed forms of presynaptic plasticity in the mature CNS is mediated by retrograde endocannabinoid (eCB) signaling (Castillo et al., 2012; Kano et al., 2009). eCBs are lipids mobilized by postsynaptic activity that travel backward across the synapse and bind presynaptic $G_{i/o}$ -coupled type-1 cannabinoid (CB_1) receptors to suppress neurotransmitter release. In the hippocampus, CB_1 receptors are highly expressed on GABAergic inhibitory interneuron axon terminals where they mediate both short-term and long-term plasticity. Short-term plasticity in the form of depolarization-induced suppression of inhibition (DSI) typically lasts less than a minute and is likely due to a transient reduction of presynaptic calcium influx (Kano et al., 2009). Long-term depression of inhibition (iLTD) involves more sustained CB_1 activation (Chevalleyre and Castillo, 2003), downregulation of PKA (Chevalleyre et al., 2007), and a long-lasting reduction in GABA release. How eCBs control neurotransmitter release during long-term plasticity is incompletely understood. Although striatal eCB-LTD was reported to involve translation (Adermark et al., 2009; Yin et al., 2006) but see (Jung et al., 2012), the mechanism that triggers protein synthesis remains unknown. Furthermore, direct evidence that CB_1 activation leads to protein synthesis is unavailable.

To determine the role of presynaptic protein synthesis in iLTD, we performed long-term paired electrophysiological recordings on synaptically connected inhibitory interneurons and CA1 pyramidal cells in acute rodent hippocampal slices, where local microcircuits are intact. Using single-cell manipulations to block protein translation, we found that iLTD requires protein

synthesis exclusively in presynaptic interneurons, most likely in axons. We also show that CB₁ activation increases protein synthesis in an mTOR-dependent manner, and that iLTD involves cap-dependent translation. Moreover, using stochastic optical reconstruction microscopy (STORM), we provide evidence that eukaryotic ribosomes are localized inside CB₁-expressing interneuron axon terminals. Our findings establish that presynaptic protein synthesis controls neurotransmitter release during long-term plasticity in the mature mammalian CNS.

Results

Long-term, but not short-term, eCB-mediated plasticity requires protein synthesis

To assess if eCB-mediated iLTD involves protein synthesis, we first elicited heterosynaptic iLTD (Chevalleyre and Castillo, 2003) by theta-burst stimulation (TBS) of presynaptic inputs onto whole-cell voltage clamped CA1 pyramidal cells in acute hippocampal slices. Compared with interleaved controls, acute bath application of either cycloheximide or anisomycin, two mechanistically distinct inhibitors of eukaryotic ribosome peptide elongation, impaired iLTD (**Figure 1A**). iLTD can also be triggered with postsynaptic activity such as multiple episodes of DSI (mDSI) (Younts et al., 2013). Compared with controls, acute bath application, but not postsynaptic loading of cycloheximide (Yin et al., 2006) or anisomycin, blocked mDSI-iLTD (**Figure 1B**), suggesting that postsynaptic translation is dispensable for iLTD. Neither cycloheximide nor anisomycin affected the magnitude or duration of short-term plasticity triggered with DSI (**Figure 1C,D**), indicating that eCB release and CB₁ activation properly function when blocking protein synthesis. Using fluorescent non-canonical amino acid tagging (FUNCAT), a technique that permits visualization of newly synthesized proteins (Dieterich et al., 2010), we confirmed that cycloheximide and anisomycin block translation in slices (**Figure 1E,F**). Taken together, these results show that protein translation is essential for long-term, but not short-term, inhibitory plasticity.

Protein synthesis is required for the induction, but not maintenance, of iLTD

Bypassing eCB production and directly activating presynaptic CB₁ with the selective agonist WIN 55,212-2 (WIN) induces chemical-iLTD (Chevalleyre and Castillo, 2003; Chevalleyre et al., 2007; Heifets et al., 2008). Using extracellular field inhibitory postsynaptic potential (fIPSP) recordings from the cell body layer, we found that WIN paired with presynaptic activity triggered

iLTD (Heifets et al., 2008), which was expressed presynaptically as reflected by an increased paired-pulse ratio (i.e. reduced release probability, P_r) (**Figure 2A**). Cycloheximide or anisomycin abolished iLTD and the associated change in P_r (**Figure 2A**). To address whether translation is necessary for the induction or maintenance of iLTD, we acutely exposed slices to cycloheximide during or after CB_1 activation and found that protein synthesis was not required during the maintenance-phase of iLTD (**Figure 2B**). Neither cycloheximide nor anisomycin affected basal inhibitory synapse strength (**Figure 2C**), indicating that protein synthesis is specifically required for long-term plasticity, and that constitutive protein synthesis does not significantly alter GABA release. As expected, iLTD was prevented in slices exposed to the selective CB_1 inverse agonist/antagonist AM251 or SR 141716 (**Figure 2D**). We also examined the potential contribution of mRNA transcription to iLTD. iLTD remained intact when transcription was blocked with actinomycin-D (**Figure S1A**), and actinomycin-D efficacy was confirmed using RT-PCR in slices (**Figure S1B**). Collectively, these findings indicate that protein synthesis, and not transcription, is required for the induction, but not maintenance, of iLTD.

CB₁ activation enhances protein translation

Given that CB_1 -mediated iLTD requires protein synthesis, we next tested whether CB_1 activation can promote translation. To increase the likelihood of detecting and quantifying potential CB_1 -mediated changes in protein synthesis, we used FUNCAT on cultured primary hippocampal neurons. Cultured neurons mainly express CB_1 in axons, but unlike inhibitory interneurons *in situ*, they also express CB_1 in soma and dendrites (Irving et al., 2000; Twitchell et al., 1997). Using MAP2 labeling to identify neurons, we found that WIN increased translation (**Figure 3A,B**). Co-application of WIN with AM251 abolished this effect (**Figure 3A,B**), indicating that CB_1 activation triggered translation. AM251 treatment alone did not significantly change the

FUNCAT signal (**Figure 3A,B**), suggesting that basal CB₁ signaling is not coupled to protein synthesis. As expected, the WIN-induced increase in FUNCAT signal was greatly reduced by cycloheximide. Using the selective agonist DHPG, we confirmed that group I metabotropic glutamate receptors (mGluRs) engage protein synthesis (Huber et al., 2000), indicating the FUNCAT assay worked as intended. We also assessed protein translation in CB₁-expressing axons and found that the FUNCAT signal in the presence of WIN was reduced by AM251 (**Figure 3C**). We conclude that neuronal CB₁ activation increases newly synthesized protein in neurons and axons.

Presynaptic CB₁-mediated iLTD requires mTOR signaling and cap-dependent translation

CB₁ can signal via the mammalian target of rapamycin (mTOR), p38 mitogen-activated protein kinase (MAPK), and/or MAPK/extracellular signal-regulated kinase (ERK) pathways (Howlett et al., 2002). Each of these pathways is known to regulate protein synthesis and play a role in postsynaptic forms of LTP and LTD (Buffington et al., 2014; Santini et al., 2014). To test if CB₁ activation increases protein synthesis in an mTOR-dependent manner, we measured translation using FUNCAT in primary neurons and found that the mTOR selective inhibitor torin-2 abolished the WIN-induced increase in translation (**Figure 4A,B**). Application of torin-2 alone had no significant effect on protein synthesis suggesting that mTOR does not regulate constitutive protein synthesis (**Figure 4A,B**). To examine whether mTOR plays a role in iLTD, we triggered iLTD in acute hippocampal slices. Compared with interleaved controls, torin-2 abolished synaptically (**Figure 4C**) and chemically-induced iLTD (**Figure 4D**). Similar to protein synthesis (**Figure 2B**), mTOR signaling was required during the induction, but not maintenance, of iLTD (**Figure 4D**). Notably, torin-2 alone did not affect basal inhibitory synapse strength ($104.5 \pm 2.2\%$ of baseline, $n = 4$, $p = 0.19735$, paired t-test, data not shown), suggesting that constitutive

mTOR signaling does not modify basal GABA release. In addition, a different mTOR inhibitor, rapamycin, impaired iLTD (**Figure 4E**). We further examined the contribution of cap-dependent protein synthesis to iLTD. Chemical-iLTD was blocked in slices exposed to 4EGI-1 (**Figure 4E**), which disrupts the eukaryotic initiation factor 4F (eIF4F) complex at the level of eIF4E and eIF4G (Moerke et al., 2007), as well as ISRIB (**Figure 4E**), which interferes with translation initiation by preventing the effects of phosphorylated eIF2 α (Sekine et al., 2015). Neither 4EGI-1 nor ISRIB alone had a significant effect on basal inhibitory fIPSP amplitude (4EGI-1: $106.4 \pm 8.0\%$ of baseline, $n = 4$; $p = 0.48092$, paired t-test; ISRIB: $96.2 \pm 2.6\%$ of baseline, $n = 7$, $p = 0.1974$, paired t-test, data not shown), further signifying that the effects of blocking translation were specific to long-term plasticity. We found a partial block of iLTD in slices treated with the p38 MAPK inhibitor SB 202190 whereas the ERK/MAPK inhibitor U-0126 had no effect (**Figure 4E**). Collectively, our results demonstrate that CB₁ activation drives protein synthesis in an mTOR-dependent manner and that cap-dependent translation is essential for iLTD.

Presynaptic, but not postsynaptic, cap-dependent translation is critical for iLTD

To directly test a role for presynaptic protein synthesis in iLTD at the single-cell level, we performed long-term paired electrophysiological recordings (up to 5 hrs) between individual hippocampal interneurons and CA1 pyramidal cells. Paired recordings allow independent control over presynaptic and postsynaptic signaling, thereby providing a means to study neurotransmitter release from fully developed GABAergic synaptic terminals in an intact circuit. Protein synthesis was inhibited at the single-cell level using the small molecule, membrane impermeable inhibitor, M⁷GpppG (M7). M7 is an mRNA cap analog that competes with endogenous 7-methyl guanosine 5'-capped mRNAs for binding to eIF4E, one of several proteins comprising the eIF4F complex that regulates cap-dependent translation (Sonenberg

and Hinnebusch, 2009). Excess M7 has been used previously to disrupt translation-dependent forms of long-term plasticity (Beaumont et al., 2001; Huber et al., 2000). To test whether iLTD requires presynaptic protein synthesis, M7 was loaded via the patch pipette directly into regular-spiking, DSI-sensitive and therefore CB₁-expressing interneurons (**Figure 5A**). Remarkably, loading M7 presynaptically for >1 hr abolished iLTD (**Figure 5B,C, Figure S2A**). We quantified GABA release during the baseline and after inducing iLTD in three ways: neurotransmitter release probability (P_r ; calculated as the number of synaptic release events, i.e. the inverse failure rate); synaptic efficacy (a measure of synaptic strength calculated by averaging all synaptic events including responses and failures); and synaptic potency (which is the average of only synaptic responses). P_r , synaptic efficacy (**Figure 5B,C**), and potency (baseline: 34.5 ± 12.8 pA vs. after iLTD induction: 31.8 ± 11.0 pA, $n = 6$; $p = 0.50625$, paired t-test, data not shown) remained stable (for up to 3 hrs) after attempting to induce iLTD. These results reinforce the idea that disrupting constitutive presynaptic protein synthesis does not alter basal GABA release. M7 did not alter physiological parameters of interneurons such as resting membrane potential (M7 loaded presynaptically: -62.9 ± 1.9 mV vs. M7 not loaded presynaptically: -62.1 ± 1.8 mV; $p = 0.73584$, unpaired t-test, $n = 6$ each) or input resistance (M7 loaded presynaptically: 275.4 ± 42.0 M Ω vs. M7 not loaded presynaptically: 231.5 ± 51.5 M Ω ; $p = 0.52464$, unpaired t-test, $n = 6$ each). These results establish that presynaptic protein synthesis is critical for iLTD, and further support a mechanism involving cap-dependent protein synthesis.

To examine the contribution of postsynaptic translation to presynaptic plasticity, M7 was loaded into CA1 pyramidal cells. As predicted, iLTD remained intact (**Figure 5D-F, Figure S2A**). The magnitude of iLTD, reflected in the P_r and synaptic efficacy measurements, was not significantly different from our previous experiments in which M7 was not present (Younts et al., 2013). Consistent with multivesicular release from these terminals (Biro et al., 2006), synaptic potency

also was reduced (baseline: 34.5 ± 11.7 pA vs. after iLTD induction: 16.8 ± 6.0 pA, $n = 6$, $p = 0.03423$, paired t-test, data not shown). These experiments indicate that iLTD does not “wash-out” of presynaptic or postsynaptic compartments because iLTD was induced in recordings in which the baseline exceeded 1 hr. Notably, iLTD was still CB₁-dependent when postsynaptic translation was blocked with M7 (**Figure S2B**), signifying that blocking *postsynaptic* protein synthesis does not alter eCB production or CB₁ signaling required for inducing iLTD. To validate that M7 worked as intended, we assessed the well-characterized, protein synthesis-dependent mGluR-LTD at excitatory Schaffer collateral-to-CA1 pyramidal cell synapses (Huber et al., 2000), and found that mGluR-LTD, triggered chemically with DHPG, was not observed when M7 was loaded postsynaptically for ~30 min (**Figure S2C**). These results demonstrate that postsynaptic translation is dispensable for iLTD.

Somatic protein synthesis in presynaptic interneurons is dispensable for iLTD

Given that CB₁ is predominantly localized to hippocampal interneuron axons and terminals *in situ* (Dudok et al., 2015; Katona et al., 1999), that iLTD is expressed presynaptically as reduced GABA release (Castillo et al., 2012), and that loading M7 into interneurons blocked iLTD (**Figure 5A-C, Figure S2A**), we hypothesized that translation is required locally in axons and/or terminals that are remote from the interneuron cell body. Consistent with this hypothesis, we found a significant positive correlation between the amount of time M7 was loaded presynaptically and the likelihood of blocking iLTD (**Figure S3A**), suggesting M7 must diffuse into remote axonal compartments to exert its blocking effect. For the experiments in which M7 was omitted from the presynaptic interneuron, the magnitude of iLTD remained stable and no correlation was observed (**Figure S3A**). To determine if M7 can diffuse into remote axons at times matching iLTD block, we used two-photon fluorescence microscopy to track the diffusion

of two fluorescent molecules, Alexa Fluor-594 and Lucifer yellow, which are similar in size to M7 (i.e. M7 proxies). We readily detected M7 proxies in putative axons (**Figure S3B,C**). To test the hypothesis that somatic translation in interneurons is dispensable for iLTD, we performed paired recordings and loaded the type-1 ribosome inactivating toxin, gelonin, which irreversibly interferes with protein elongation, into regular-spiking, DSI-sensitive interneurons. Given its relatively large size (~30 kDa), we reasoned that gelonin introduced via the patch pipette would be relatively restricted to the soma and proximal neurites and therefore less effective at blocking translation in distal axon terminals. We could only detect gelonin (3-30 μ M, labeled with Alexa Fluor-488) in somata and proximal dendrites but not in putative axons (**Figure S3B,C**). Functionally, gelonin (3 μ M) loaded presynaptically for 105.3 ± 4.9 min failed to block iLTD (**Figure 6A,B**). To assess if gelonin blocked somatic translation, we loaded gelonin (3 μ M) for ~30 min into one of two neighboring CA1 interneurons in slices and performed FUNCAT (**Figure 6C,D**). Gelonin substantially reduced somatic translation in these interneurons (**Figure 6C,D**). As a functional positive control in interleaved experiments, we found that gelonin (3 μ M) loaded postsynaptically for ~30 min readily blocked mGluR-LTD at excitatory synapses onto CA1 pyramidal cells (**Figure 6E**). Finally, we examined the possibility that a somatically synthesized protein might traffic along microtubules into axonal compartments during iLTD. Slices were pre-incubated and continuously perfused with the microtubule depolymerizing agent colchicine (for up to 5 hrs) or nocodazole (for up to 8 hrs). These reagents had no effect on iLTD (**Figure 6F**) or intrinsic membrane properties (**Figure S4A**), despite nocodazole disrupting neuronal microtubule integrity in slices as measured with second harmonic generation microscopy (**Figure S4B,C**). These observations suggest that microtubule-based trafficking mechanisms do not participate in iLTD. Taken together, these results indicate that somatic translation and transport are not required for iLTD, strongly suggesting that iLTD involves presynaptic protein synthesis in axons.

Anatomical evidence for ribosomes in mature mammalian axon terminals

If iLTD involves presynaptic protein synthesis, then ribosomes should be present in CB₁-expressing interneuron axons and terminals. To visualize ribosomes specifically within this interneuron type, we co-immunostained mouse and rat hippocampal slices using antibodies specific for CB₁ and ribosomes. We and others have previously validated the CB₁ antibody (Dudok et al., 2015; Fukudome et al., 2004). The Y10b antibody is also well-characterized and validated, recognizing 5.8S non-coding ribosomal RNA in the 60S subunit. Consistent with previous reports (Dudok et al., 2015; Katona et al., 1999), confocal imaging revealed a characteristically dense network of CB₁-expressing basket-like axons and preterminal axon segments encircling CB₁-immunonegative CA1 pyramidal cell bodies (**Figure 7A, Figure S5A**). As expected, there was high ribosome density expressed in the perinuclear cytoplasm of CA1 pyramidal cell bodies (**Figure 7A, Figure S5A**). With the exception of nucleoli (not shown), where 5.8S rRNA is made and spliced, the nucleus was nearly devoid of 5.8S rRNA. We validated Y10b staining by treating sections with RNase A and micrococcal nuclease enzymes, which degrade RNA and thus the Y10b epitope. Compared with control, sections pretreated with nucleases had substantially less Y10b labeling (**Figure 7A, Figure S5A,B**).

In an effort to detect ribosomes in CB₁-expressing axon terminals, we performed 3D STORM imaging (Huang et al., 2008). Using a recently developed combined STORM/confocal imaging approach that reliably measures CB₁ position in the plasma membrane (Barna et al., 2016; Dudok et al., 2015), we visualized 5.8S rRNA molecules within CB₁-expressing axon terminals (**Figure 7B**) located in the somatic and dendritic fields of CA1 (**Figure S5B**). Nuclease pretreatment largely eliminated 5.8S rRNA immunostaining from these terminals (**Figure 7A,D,**

Figure S5B). In a complementary set of experiments, we immunolabeled ribosomal protein S6 (rpS6), which is an integral component of the eukaryotic 40S ribosomal subunit and an effector of mTOR signaling. rpS6 molecules were also readily visualized with STORM imaging inside CB₁-expressing axon terminals (**Figure 7C**, **Figure S5C**). The densities of 5.8S rRNA (**Figure 7D**) and rpS6 protein (**Figure 7E**) puncta were significantly higher (by ~90%) in axon terminals compared to the corresponding background signal measured from CA1 pyramidal cell nuclei. Preterminal axon segments exhibited an intermediate labeling density. Quantitative nanoscale analysis showed an identical clustering distribution for 5.8S rRNA and rpS6 localization points within CB₁-expressing axon terminals (**Figure 7F**), and dual channel STORM revealed co-clustering of 5.8S rRNA and rpS6 molecules in these boutons (**Figure S6A-C**). The mean number (\pm standard deviation) of 5.8S rRNA and rpS6 clusters per bouton was 3.34 ± 0.79 and 2.92 ± 1.16 , and the percentage of ribosome-containing boutons was $91 \pm 7\%$ and $83 \pm 18\%$, respectively. As expected, CB₁-expressing axon terminals containing the presynaptic active zone protein bassoon also showed ribosomal labeling (**Figure S6D-G**). Presynaptic 5.8S rRNA STORM signal was observed in CB₁-expressing axon terminals from rat hippocampal sections, and signal specificity was confirmed in nuclease-treated sections (control, $n = 57$ boutons vs. nuclease treatment, $n = 56$ boutons, 2 animals each, $p < 0.0001$, Mann-Whitney U test, data not shown). Interestingly, presynaptic ribosomal labeling was also detected in parvalbumin-positive inhibitory interneuron boutons (**Figure S7**). The number of 5.8S rRNA and rpS6 clusters per bouton was 2.41 ± 0.84 and 2.42 ± 1.03 , and the percentage of ribosome-containing boutons was $82 \pm 11\%$ and $77 \pm 14\%$, respectively. Jointly, these data provide strong anatomical support for eukaryotic ribosomes in mammalian axon terminals of inhibitory interneurons.

To determine the nanodomain distribution of ribosomes within presynaptic CB₁-expressing interneuron terminals, we employed dual-channel 3D directSTORM imaging. We previously

established that CB₁ localization points, which delimit the presynaptic bouton, can be fit with a convex hull with nanoscale precision (Dudok et al., 2015), thereby defining the membrane of the axon terminal (**Figure 7H**). Dual-STORM imaging uncovered 5.8S rRNA within CB₁-expressing axon terminals (**Figure 7G,H**). Quantitative nanoscale distribution analysis uncovered a high density of 5.8S rRNA within the presynaptic terminal just inside the plasma membrane (**Figure 7G, Figure S6D-G**). The density of 5.8S rRNA just outside the presynaptic plasma membrane, corresponding to the synaptic cleft and interstitial space, was virtually zero (**Figure 7G**). Taken together, these findings provide molecular and anatomical evidence for the presence of presynaptic ribosomes inside CB₁-expressing interneuron terminals.

Discussion

We established that presynaptic protein synthesis is essential for a presynaptically-expressed form of long-term plasticity in the mature mammalian brain. We found that CB₁ activation generates new proteins, and that iLTD likely requires axonal protein synthesis independent of somatic translation, transcription, and microtubule-based trafficking mechanisms. Our combined molecular and anatomical approach revealed eukaryotic ribosomes in fully-developed CB₁-expressing interneuron axon terminals. Mechanistically, CB₁ activation drives the cap-dependent translation machinery via the mTOR pathway. Translation plays a specific role in long-term plasticity since disrupting translation initiation or peptide elongation did not affect basal GABA release or short-term plasticity. We also report that protein synthesis is required for the induction, but not maintenance, of iLTD. These findings converge on a novel model whereby presynaptically synthesized proteins act as a molecular switch to persistently reduce GABA release from inhibitory interneuron terminals.

Neurons must coordinate gene expression at thousands of synapses distant from their soma. Local translation can impart axons and dendrites with computational autonomy to rapidly respond to the environment, independent of the soma (Alvarez et al., 2000; Holt and Schuman, 2013; Jung et al., 2014). The concept of local presynaptic protein synthesis was first proposed nearly 50 years ago (for a thorough review, see Alvarez et al., 2000). Presynaptic local protein synthesis during long-term plasticity has since been demonstrated in non-mammalian preparations such as crayfish (Beaumont et al., 2001), sea slug (Martin et al., 1997), frog (Zhang and Poo, 2002), and leech (Yuan and Burrell, 2013). An advantage of these preparations is that the presynaptic axons are relatively large and can be directly manipulated via pressure-injection of translation inhibitors. In contrast, mammalian axons are much smaller

and therefore more difficult to access. Previous research in rodents has so far relied on non-physiological treatments such as axotomy or non-specific manipulations such as blocking postsynaptic protein synthesis to infer a role for presynaptic translation during long-term plasticity (Barnes et al., 2010; Calixto et al., 2003; Hagena and Manahan-Vaughan, 2013; Huang and Hsu, 2004; Huang et al., 1994; Kelly et al., 2000; Yin et al., 2006). Protein synthesis can be upregulated in response to injury or occur in neighboring neurons or glia. We used long-term paired recordings and single-cell manipulations in a locally intact circuit to demonstrate that presynaptic, likely axonal, protein synthesis is essential for regulating neurotransmitter release during long-term plasticity. Our findings also indicate that presynaptic protein synthesis during long term-plasticity is evolutionarily conserved from invertebrates to mammals.

The presence of ribosomes has been well documented in mammalian axonal growth cones, regenerating axons, and peripheral sensory axons (Crispino et al., 2014; Jung et al., 2014). However, failure to detect ribosomes in mature mammalian CNS axons (Palay and Palade, 1955), and the observation that neuronal somata can source protein to axons (Droz and Leblond, 1963), likely gave rise to the notion that presynaptic compartments in the mature mammalian brain do not synthesize proteins. This dogma persisted despite ribosomes being identified in axon initial segments of mammalian cortical principal cells (Jones and Powell, 1969; Steward and Ribak, 1986) and spinal nerves (Koenig et al., 2000). Ribosome-associated proteins, initiation and elongation factors have now been detected in whole-brain presynaptic bouton preparations (Wilhelm et al., 2014), and hundreds of mRNA transcripts encoding presynaptic proteins were isolated from cultured cortical axons (Taylor et al., 2009), hippocampal slices of CA1 neuropil (Cajigas et al., 2012), and retinal ganglion cell axons *in vivo* (Shigeoka et al., 2016). In addition, axonal protein synthesis has recently been linked with synaptic transmission and axon maintenance (Shigeoka et al., 2016; Yoon et al., 2012), which

may be dysregulated in Alzheimer's disease (Baleriola et al., 2014) and Fragile X Syndrome (Akins et al., 2012; Christie et al., 2009). These studies and ours collectively raise the strong possibility that the soma is not the exclusive origin of presynaptic proteins. Further, our work establishes that presynaptic ribosomes play a functional role in presynaptic long-term plasticity.

Our findings using various protein synthesis inhibitors suggest that presynaptic CB₁-expressing interneuron terminals contain eukaryotic ribosomes. We used super-resolution STORM microscopy to provide direct evidence for ribosomes in axonal boutons and to quantify, in a cell-type- and synapse-specific manner, their nanoscale spatial distribution. We found a high density of ribosomes within 25-400 nm of the presynaptic plasma membrane, where they are positioned to integrate CB₁ signaling. It is unclear why previous ultrastructural studies in mature CNS axons failed to detect ribosomes in synaptic terminals. Presumably, those studies lacked sufficient sensitivity to detect ribosomes or focused exclusively on excitatory synapses. Alternatively, ribosomes in certain presynaptic terminals may be disassembled and thus go undetected until an external cue (e.g. activity or receptor ligand) initiates translation (Tcherkezian et al., 2010). It is also conceivable that certain presynaptic terminals express unconventional ribosomes (Xue and Barna, 2012). Regardless of the underlying biological or technical explanation, our study demonstrates that eukaryotic ribosomes are present in fully mature CNS inhibitory interneuron terminals.

CB₁ can transduce signals to several downstream effectors including voltage-gated Ca²⁺ and K⁺ channels, PKA, ERK/MAPK, p38-MAPK, and PI3K (Howlett et al., 2002). Many of these signaling cascades were originally characterized in heterologous overexpression systems. Thus, the precise pathways engaged by CB₁ in intact preparations remain unclear. A previous

study reported that CB₁ activation can indirectly upregulate mTOR signaling, presumably in *postsynaptic* compartments (Puighermanal et al., 2009). Instead, we found that both synaptically- and chemically-induced iLTD are coupled to mTOR, suggesting that mTOR signaling operates in *presynaptic* compartments. Using FUNCAT in cultured hippocampal neurons, we also directly showed that CB₁ activation leads to new protein synthesis in an mTOR-dependent manner. To our knowledge, this is the first demonstration that CB₁ activation causes an overall increase in protein synthesis. Though it is presently not possible to distinguish between a requirement for constitutive and/or *de novo* protein synthesis during forms of plasticity in which target protein(s) remain unidentified, mTOR can control eIF4F-mediated cap-dependent translation initiation, a highly regulated and rate-limiting step (Sonenberg and Hinnebusch, 2009). Given our findings that eIF4F is critical for iLTD, these results imply that CB₁ activation enhances the rate of protein synthesis. Novel methods with improved spatiotemporal resolution need to be developed to reveal *de novo* protein synthesis at presynaptic terminals in brain tissue.

Protein synthesis is commonly linked to the maintenance of long-term plasticity (Buffington et al., 2014; Santini et al., 2014). We found that blocking translation right after inducing iLTD had no effect on long-term plasticity. This observation is consistent with our previous work indicating CB₁ activation is required during the induction, but not maintenance, of iLTD (Chevalleyre and Castillo, 2003). Given that CB₁ receptors enhance translation, the newly synthesized protein(s) may act as a functional molecular switch to inhibit neurotransmitter release and therefore trigger long-term, but not short-term, plasticity. Once the protein(s) are synthesized and iLTD is established, protein translation is no longer required to maintain the synapse in a depressed state (Klein et al., 2015). While additional research is needed to identify exactly which protein(s) are synthesized, candidates include the translation machinery itself, synaptic vesicle-associated

signaling proteins, and structural proteins linked with the cytoskeleton, active zone, and intercellular adhesion. There is evidence that actin can be locally synthesized in axon growth cones, sensory axons, and cultured CNS axons (for reviews, see Gomes et al., 2014; Jung et al., 2014), and that CB₁ activation leads to cytoskeletal rearrangements including axon growth cone collapse/expansion (Argaw et al., 2011; Berghuis et al., 2007; Njoo et al., 2015; Roland et al., 2014). Synthesis of a structural/cytoskeletal protein could increase the coupling distance between presynaptic calcium channels and the active zone to efficiently suppress GABA release.

The impact of iLTD manifests at the circuit level. CB₁ receptors expressed on the axon terminals of interneurons can persistently gate excitation via somatic and dendritic disinhibition (Basu et al., 2013; Younts et al., 2013). *In vivo* studies suggest that redistribution of inhibitory interneuron spiking and spike-timing can reconfigure ensembles of active hippocampal pyramidal cells in space and time (Dupret et al., 2013; Klausberger et al., 2005). We propose that presynaptic translation in inhibitory interneurons helps orchestrate the excitability of a subset of pyramidal cells in specific circuits established during the learning processes. Given the important role of protein synthesis in cognitive functions (Buffington et al., 2014; Santini et al., 2014), our results also warrant consideration in the context of dysregulated translational control and inappropriately balanced excitation and inhibition. Dysregulated translation in inhibitory interneurons may be an overlooked mechanism in brain disorders (Buffington et al., 2014; Darnell and Klann, 2013).

Experimental Procedures

See Supplemental Experimental Procedures for detailed methods.

Slice preparation and electrophysiology

Acute transverse hippocampal slices (400 μm thick) were prepared from male and female (P15-30) Sprague Dawley rats and C57BL/6 mice using standard procedures approved by NIH and Albert Einstein College of Medicine Institutional Animal Care and Use Committee guidelines. Whole-cell voltage and current clamp recordings were performed with an Axon MultiClamp 700B amplifier (signals filtered at 2 kHz and digitized at 5 kHz). Stimulation and acquisition were controlled with custom software (Igor). Stock reagents were prepared according to the manufacturer's recommendation. All experiments were performed in an interleaved fashion. "n" represents number of independent cells or field recordings in slices.

FUNCAT and image analysis

Acute hippocampal slices (400 μm thick) or primary hippocampal neurons (from E18-19 rats and grown *in vitro* for 18 days) were prepared using standard procedures. Slices were treated with reagents as described and then exposed to azidohomoalanine (AHA) for 2.5 hrs before fixation. Neuron cultures were pre-incubated with methionine-free medium for 30 min, then incubated with AHA for 1.5 hrs and treated with reagents, as described. Following the Click-it® reaction, immunocytochemistry was performed. Images were obtained using the same settings for all samples within an experiment. Experimenter was blind to the treatment condition. Image processing was performed with ImageJ (NIH).

STORM microscopy and image analysis

Experimental procedures were approved by the Hungarian Committee of the Scientific Ethics of Animal Research. Acute hippocampal slices (300 μm thick) were prepared from male Sprague-Dawley rats and C57BL/6N mice (P30-40) according to standard procedures. Tissue processing, immunostaining, and imaging was performed as described (Barna et al., 2016; Dudok et al., 2015). After data acquisition, the confocal images were deconvolved. Identification of single-molecule localization points was performed with NIS-Elements N-STORM module (Nikon). Correlated analysis of confocal and STORM images was performed in VividSTORM. Localization precision was measured from the standard deviation of coordinates in isolated clusters (Dudok et al., 2015) at 13 nm and 34 nm in the lateral and axial dimensions, respectively. The localization accuracy for determining the position of one blinking event was 6.8 nm with single channel STORM and 10.6 nm with dual-channel STORM. Three-dimensional STORM renderings of localization points were constructed using Visual Molecular Dynamics software. All images within each experiment were processed in parallel using identical imaging and analysis conditions.

Statistics

Summary data are presented as mean \pm standard error of mean (SEM), unless otherwise indicated. Significance ($p < 0.05$) was assessed with one-way ANOVA (means comparison with *post hoc* Bonferroni test for electrophysiology and FUNCAT, or Tukey test for STORM), Student's paired and unpaired t-tests, Wilcoxon matched-pairs signed rank test, Mann Whitney U-test, or Pearson's correlation coefficient, as indicated.

Figure Legends

Figure 1. Synaptically-induced iLTD involves protein synthesis.

(A) Whole-cell recordings from CA1 pyramidal cells in acute slices. Presynaptically-induced iLTD was blocked by acute bath application of cycloheximide (cyclo, 80 μ M) or anisomycin (aniso, 20 μ M) (washed-out after the induction). Arrow, TBS protocol. For all electrophysiology figures, representative traces (1) and (2) correspond to the gray shaded areas (1) and (2) in the summary time-course plots. Control: $73.1 \pm 2.1\%$ vs. cyclo: $91.4 \pm 3.8\%$ vs. aniso: $89.0 \pm 5.1\%$; $F[2,20] = 11.17646$; $p = 0.00055$, one-way ANOVA. $n =$ number of cells.

(B) Postsynaptically-induced iLTD was inhibited by acute bath application of cyclo (80 μ M) or aniso (20 μ M) (washed out after the induction). Except for control, cyclo (80 μ M) or (20 μ M) aniso was loaded postsynaptically via the patch pipette for all experiments. Black bar, mDSI protocol. Control: $74.3 \pm 3.4\%$ vs. cyclo or aniso loaded postsynaptically: $84.8 \pm 2.2\%$ vs. cyclo: $102.5 \pm 5.2\%$ vs. aniso: $109.6 \pm 5.3\%$; $F[3,28] = 18.99148$; $p < 0.00001$, one-way ANOVA. Control vs. cyclo or aniso loaded postsynaptically; $p = 0.00135$, unpaired t-test.

(C) Short-term eCB-mediated plasticity elicited with DSI was not affected by cyclo (80 μ M). Arrow, DSI protocol. Control: $63.6 \pm 2.4\%$ vs. cyclo: $69.5 \pm 3.1\%$; $p = 0.18284$, unpaired t-test. Slices were exposed to cyclo for no more than 1 hr.

(D) Similar to panel C but for aniso (20 μ M). Control: $68.3 \pm 3.0\%$ vs. aniso: $66.4 \pm 2.8\%$; $p = 0.65988$, unpaired t-test.

(E) Cyclo (80 μ M) and aniso (20 μ M) blocks translation in slices as reflected by reduced FUNCAT signal in representative confocal images of the CA1 cell body layer.

(F) Summary data. FUNCAT fluorescence intensity, in arbitrary units, normalized to control. Control: 1.00 ± 0.03 (7 slices) vs. cyclo: 0.44 ± 0.02 (5 slices) vs. aniso: 0.62 ± 0.02 (3 slices); $F[2,216] = 116.10$; $***p < 0.001$, one-way ANOVA. Regions of interest (ROIs) were randomly selected from somata. Numbers in parenthesis refer to number of ROIs analyzed (i.e. 5 somas/image and ~ 3 images/slice).

(A-D): Data are shown as mean \pm SEM.

Figure 2. Presynaptic CB₁-mediated iLTD requires translation during the induction-phase.

(A) fIPSP recordings in acute hippocampal slices. Top panel: chemically-induced iLTD (WIN 5 μ M + activity, black bars) was blocked by bath application of cyclo (80 μ M) or aniso (20 μ M) (washed out after the induction). Control: $77.8 \pm 2.4\%$ vs. cyclo: $100.6 \pm 3.9\%$ vs. aniso: $99.2 \pm 6.6\%$; $F[2,21] = 11.30053$; $p = 0.00047$, one-way ANOVA. SR 141716 (5 μ M), a CB₁ inverse agonist/antagonist was bath applied after WIN to terminate CB₁ activation. Picrotoxin (bath applied at end of experiment) confirms fIPSPs were GABA_A receptor-mediated. Bottom panel: translation inhibitors blocked the increased paired-pulse ratio (PPR) associated with iLTD. Control: $112.5 \pm 3\%$ vs. cyclo: $102.2 \pm 1.3\%$ vs. aniso: $101.3 \pm 3.4\%$; $F[2,21] = 5.66567$; $p = 0.01077$, one-way ANOVA. Gray and white bars signify presence of translation inhibitors. Data in both panels from same recordings. $n =$ number of slices.

(B) Protein synthesis was required during the induction, but not maintenance, of iLTD. Slices were acutely exposed to cyclo (80 μ M) during min -25 to 25 (gray bar) or min 25 to 75 (white bar). Control: $74.5 \pm 5.2\%$ vs. cyclo min -25 to 25: $98.6 \pm 5.2\%$ vs. cyclo min 25 to 75: $82.4 \pm 4.2\%$; $F[2,19] = 5.71536$; $p = 0.01002$, one-way ANOVA.

(C) Neither cyclo (80 μ M) nor aniso (20 μ M) had a lasting impact on basal inhibitory synaptic transmission: cyclo: $105.1 \pm 4.0\%$ compared to baseline, $p = 0.2378$, paired t-test; aniso: $103.0 \pm 4.1\%$ compared to baseline; $p = 0.48869$, paired t-test. Inhibitors were bath applied for 50 min (black bar), as in panels A and B.

(D) AM251 (5 μ M, $n = 2$) or SR 141716 (5 μ M, $n = 2$) prevented iLTD: $101.2 \pm 3.1\%$ compared to baseline; $p = 0.82567$, paired t-test (AM251 and SR 141716 results pooled because there was no difference). Slices pre-incubated (>1 hr) and continuously perfused with CB₁ blockers.

Data are shown as mean \pm SEM.

Figure 3. CB₁ activation increases protein synthesis in neurons

(A) Representative fluorescence images of FUNCAT signal acquired from primary hippocampal neurons (confirmed with MAP2 immunostaining which exclusively labels neurons) exposed for 25 min to vehicle control (DMSO), the CB₁ agonist WIN (5 μ M), WIN and AM251 (both at 5 μ M), AM251 alone (5 μ M), WIN and cyclo (5 μ M and 80 μ M, respectively), or DHPG (50 μ M, 10 min).

(B) Summary data. FUNCAT fluorescence intensity, in arbitrary units, normalized to control. Control (8 wells, 3 replicates): 1.00 ± 0.03 vs. WIN (7 wells, 3 replicates): 1.28 ± 0.04 vs. WIN + AM251 (9 wells, 2 replicates): 0.99 ± 0.03 vs. AM251 alone (3 wells, 2 replicates): 0.90 ± 0.04 vs. WIN + cyclo (4 wells, 2 replicates): 0.63 ± 0.02 vs. DHPG (9 wells, 3 replicates): 1.20 ± 0.04 (9 wells, 3 replicates); $F[5,401] = 28.09$; $**p < 0.01$, $****p < 0.0001$, one-way ANOVA. ROIs were generated from neuronal somata and neurites using MAP2. Numbers in parentheses refer to number of images analyzed (i.e. 2-8 neurons/image and \sim 5 images/well).

(C) Top panels: representative fluorescence images of FUCAT signal acquired from putative axons under CB₁-positive puncta exposed to WIN (5 μ M) and WIN + AM251 (both at 5 μ M). Bottom left: wide-field image of a neuron immunostained with CB₁ and MAP2. Arrowheads indicate putative axons containing CB₁ but lacking MAP2 staining. Right: summary data of FUNCAT fluorescence intensity, in arbitrary units, normalized to WIN + AM251. WIN (7 wells, 2 replicates): 1.42 ± 0.09 vs. WIN + AM251 (6 wells, 2 replicates): 1.00 ± 0.02 ; $U = 202$, $***p < 0.001$, Mann Whitney. Numbers in parentheses refer to number of images analyzed (i.e. 1-2 neurons/image and \sim 5 images/well).

Data represent mean \pm SEM.

Figure 4. CB₁-mediated iLTD recruits the mTOR pathway

(A) Representative fluorescence images of FUNCAT signal acquired from cultured primary hippocampal neurons exposed for 25 min to vehicle control (DMSO), WIN (5 μ M), WIN (5 μ M) and the mTOR inhibitor torin-2 (100 nM), and torin-2 alone (100 nM).

(B) Summary data. FUNCAT fluorescence intensity, in arbitrary units, normalized to control. Control (9 wells, 4 replicates): 1.00 ± 0.02 vs. WIN (7 wells, 3 replicates): 1.20 ± 0.04 vs. WIN + torin-2 (5 wells, 2 replicates): 1.02 ± 0.06 vs. torin-2 alone (6 wells, 2 replicates): 0.90 ± 0.04 . $F[3,201] = 11.90$; $***p < 0.001$, one-way ANOVA. Numbers in parentheses refer to number of images analyzed (i.e. 2-8 neurons/image and \sim 5 images/well).

(C) Whole-cell recordings in acute hippocampal slices. Presynaptically-induced TBS-iLTD was abolished by torin-2 (100 nM). Control: $70.8 \pm 4.3\%$ vs. torin-2: $94.0 \pm 3.0\%$; $p = 0.00083$, unpaired t-test. Slices pre-incubated (>1 hr) and continuously perfused with torin-2.

(D) fIPSP recordings in acute hippocampal slices. mTOR was required during the induction, but not maintenance, of chemical-iLTD. Slices were acutely exposed to torin-2 (100 nM) during min -25 to 25 or min 25 to 75. Control: $81.8 \pm 3.3\%$ vs. torin-2 min -25 to 25: $95.2 \pm 3\%$ vs. torin-2 min 25 to 75: $72.5 \pm 4.6\%$; $F[2,19] = 8.45658$; $p = 0.00236$, one-way ANOVA.

(E) Summary data for fIPSP recordings showing that mTOR and cap-dependent translation are required for chemical-iLTD. Data from panel D were replotted for comparison. iLTD was blocked in slices acutely exposed (washed out after induction) to the mTOR inhibitor rapamycin (100 nM) (control: $74.2 \pm 3.4\%$ vs. rapamycin: 91.3 ± 2.3 ; $p = 0.00054$) and the cap-dependent translation inhibitor 4EGI-1 (1 μ M) (control: $80.5 \pm 2.6\%$ vs. 4EGI-1: $100.3 \pm 3.4\%$; $p = 0.00169$). ISRIB (1 μ M), a different cap translation inhibitor, blocked iLTD in slices pre-incubated (>1 hr) and continuously perfused (control: $80.1 \pm 2.4\%$ vs. ISRIB: $95.8 \pm 4.4\%$; $p = 0.00408$). iLTD was partially blocked in slices acutely exposed (washed out after induction) to the p38 MAPK inhibitor SB 202190 (10 μ M) (control: 66.7 ± 3.9 vs. SB 202190: $79 \pm 1.2\%$; $p = 0.01661$) but not the MAPK/ERK inhibitor U-0126 (10 μ M) (control: $69.2 \pm 5.3\%$ vs. U-0126: $79.8 \pm 6.1\%$; $p = 0.13075$). The inactive form of U-0126, U-0124, was used as control. Unpaired t-tests.

Data are shown as mean \pm SEM.

Figure 5. Presynaptic cap-dependent protein synthesis is essential for iLTD

(A-C) Paired recordings in which M7 was loaded presynaptically via the patch pipette.

(A) Top: regular-spiking action potential firing pattern characteristic of DSI sensitive and thus CB₁-expressing interneurons. Middle: Representative traces collected before, during, and after DSI. Bottom: DSI summary data. DSI: $-0.8 \pm 6.2\%$ compared to baseline; $p < 0.00001$, paired t-test. uIPSC (unitary IPSC).

(B) Representative time course plot for an attempted iLTD experiment in which M7 (250 μ M) was loaded presynaptically into the interneuron for 86 min prior to inducing iLTD. Black bar, mDSI protocol. Presynaptic action potentials (averaged) and corresponding evoked uIPSCs are shown (example responses and failures in gray; averaged responses and failures in black).

(C) Summary data. (1) and (2) refer to baseline and after iLTD induction, respectively (see gray shaded areas in panel B). P_r during baseline: 0.62 ± 0.11 vs. after iLTD induction: 0.56 ± 0.12 ; $p = 0.56546$, paired t-test. Efficacy during baseline: 26.4 ± 13.2 pA vs. after iLTD induction: 23.0 ± 11.9 pA; $p = 0.48395$, paired t-test. See **Figure S2A** for time-course plots of summary data.

(D-F) Paired recordings in which M7 was loaded postsynaptically via the patch pipette.

(D) Similar to panel A. DSI: $1.1 \pm 3.9\%$ compared to baseline; $p < 0.00001$, paired t-test. Magnitude of DSI was not significantly different from that in panel A; $p = 0.90793$, unpaired t-test.

(E) Similar to panel B, but M7 (250 μ M) was loaded postsynaptically into the CA1 pyramidal cell for 40 min prior to inducing iLTD.

(F) Summary data. P_r during baseline: 0.75 ± 0.08 vs. after iLTD induction: 0.42 ± 0.09 ; $p = 0.00193$, paired t-test. Efficacy during baseline: 28.4 ± 12.3 pA vs. after iLTD induction: 8.9 ± 5.3 pA; $p = 0.04314$, paired t-test. The baseline P_r and synaptic efficacy were not different between M7 loaded presynaptically and postsynaptically experiments ($p = 0.30708$ and $p = 0.70520$, respectively, unpaired t-tests). See **Figure S2B,C** for M7 loaded postsynaptically positive control.

Data are shown as mean \pm SEM.

Figure 6. Somatic protein synthesis is dispensable for iLTD

(A) Representative iLTD time course plot for a paired recording in acute hippocampal slices in which gelonin (3 μ M) was loaded presynaptically into the CA1 interneuron for ~ 100 min prior to inducing iLTD. Black bar, mDSI protocol.

(B) Summary data. P_r during baseline: 0.71 ± 0.10 vs. after iLTD induction: 0.44 ± 0.12 ; $p = 0.02257$, paired t-test. Efficacy during baseline: 24.3 ± 8.7 pA vs. after iLTD induction: 9.0 ± 4.5 pA; $p = 0.01699$, paired t-test. The baseline P_r and synaptic efficacy were not statistically different between gelonin loaded presynaptically and M7 loaded postsynaptically, which served as control ($p = 0.64124$ and $p = 0.98827$, respectively, unpaired t-tests) (c.f. **Figure 5F**).

(C) Gelonin (3 μ M) blocks somatic translation at the single-cell level in acute hippocampal slices. Left panel: representative confocal images of two neighboring CA1 interneurons that were patched near-simultaneously and loaded via the patch-pipette with the morphological dye, lucifer yellow (2 mM). Gelonin (3 μ M) was also loaded into the cell on the right for ~ 30 min. The pipettes were gently withdrawn. Slices were then processed for FUNCAT. Middle panel: FUNCAT signal from the same slice. Right panel: merged images.

(D) Summary data and FUNCAT quantification (fluorescence intensity, in arbitrary units, normalized to control) for dual recordings. Cells were loaded for 30.0 ± 2.3 min. Control: 1.0 ± 0.0 vs. gelonin: 0.67 ± 0.09 , $p = 0.0313$, Wilcoxon matched-pairs signed rank test. Homogenous ROIs ($n = 2$) were selected from each neuronal somata ($n = 6$ slices).

(E) Whole-cell recordings in which gelonin (3 μ M) loaded postsynaptically into CA1 pyramidal cells blocked chemically-induced mGluR-LTD (DHPG, 50 μ M, 5 min, black bar). Control: $62.2 \pm 8.1\%$ vs. gelonin: $98.2 \pm 6.4\%$; $p = 0.00221$, unpaired t-test. Gelonin was loaded for 32.0 ± 2.3 min before DHPG application.

(F) Field recordings in which the microtubule depolymerizing compounds nocodazole (20 μ M) and colchicine (100 μ M) did not affect chemical iLTD. Control: $77.2 \pm 3.1\%$ vs. colchicine: $76.0 \pm 2.5\%$ vs. nocodazole: $79.8 \pm 2.0\%$; $F[2,17] = 0.72626$; $p = 0.49813$, one-way ANOVA. Slices were pre-incubated in colchicine and nocodazole for >2.5 hrs (usually ~ 4 hrs, up to 5 and 8 hrs, respectively) and continuously perfused. See **Figure S4** for nocodazole positive control. Data are shown as mean \pm SEM.

Figure 7. Ribosomes are present in CB₁-expressing interneuron axons and terminals

(A) Fixed mouse hippocampal slices were immunostained against 5.8S rRNA using the monoclonal Y10b antibody (green) and CB₁ antibody (blue). Deconvolved confocal image of 5.8S rRNA immunostaining in CA1 cell body layer reveals heavily labeled perinuclear cytoplasm of pyramidal cells (asterisks). Note the characteristically dense meshwork of axons and preterminal axon segments expressing CB₁ receptors (box). Compared with control, sections pretreated with nuclease enzymes had significantly less 5.8S rRNA immunolabeling (quantified in panel D), confirming the specificity of the antibody and labeling procedure.

(B) Representative maximum intensity volume view of correlated confocal and 3D-STORM microscopy images shows 5.8S rRNA immunolabeling inside a CB₁-expressing axon terminal (panel A, white box). An area within CB₁-expressing axon terminals was selected from the central confocal slice using an unbiased active contour algorithm (gold outline in xy plane of panels B and C). The number of STORM localization points within these ROIs was used to calculate density values for each bouton.

(C) Similar to panel B, but for ribosomal protein, rpS6. Same imaging modality as in panel B.

(D) Left panel: pretreatment with nuclease enzymes decreased STORM localization point density in CB₁-expressing axon terminals ($n = 28 \pm 2$ standard deviations, unpaired t-test). Right panel: Interneuron axon terminals ($n = 29 \pm 1$) contained significantly more ribosomal labeling compared to preterminal axon segments ($n = 13 \pm 3$) and pyramidal cell nuclei ($n = 4$), representing background staining, one-way ANOVA. Each graph shows raw data normalized to control axon terminals ($n = 3$ mice per condition).

(E) Similarly, rpS6 immunopositive STORM labeling density was significantly higher in axon terminals ($n = 21 \pm 3$) than background staining in nuclei ($n = 4$), one-way ANOVA. Preterminal segments ($n = 13 \pm 2$).

(F) Nanoscale spatial distribution of 5.8S rRNA and rpS6 immunolabeling was virtually identical (c.f. **Figure S6A-C**). Maximal clustering between pairs of localization points occurred near ~ 50 nm (note apparent clustering of points in panels B and C). ϵ refers to the Euclidian distance between point pairs that are confined by the active contour border. The y-axis refers to the number of point pairs separated by less than ϵ normalized to a randomized distribution of such point pairs for each distance. Filled symbols represent the mean and error bars the 95% confidence interval.

(G) Dual-channel 3D-STORM imaging of CB₁ and 5.8S rRNA immunolabeling shows high density of ribosomal material at the inner plasma membrane surface of CB₁-expressing axon terminals ($n = 25$ boutons, 2 mice, representative images in panel H). The outer surface of the bouton was largely devoid of 5.8S rRNA immunolabeling. The signal was present at low density in surrounding neuropil and accumulated in neighboring cells with distance from the terminals. Filled symbols are mean \pm 95% confidence interval. NLP, number of localization points.

(H) Dual-channel 3D volume renderings of two adjacent CB₁-expressing axon terminals (single arrowhead and double arrowhead) demonstrate 5.8S rRNA immunolabeling inside the convex

hull fit to CB₁ localization points (silver lines). Dotted line indicates neighboring postsynaptic neuron cell body (asterisk).

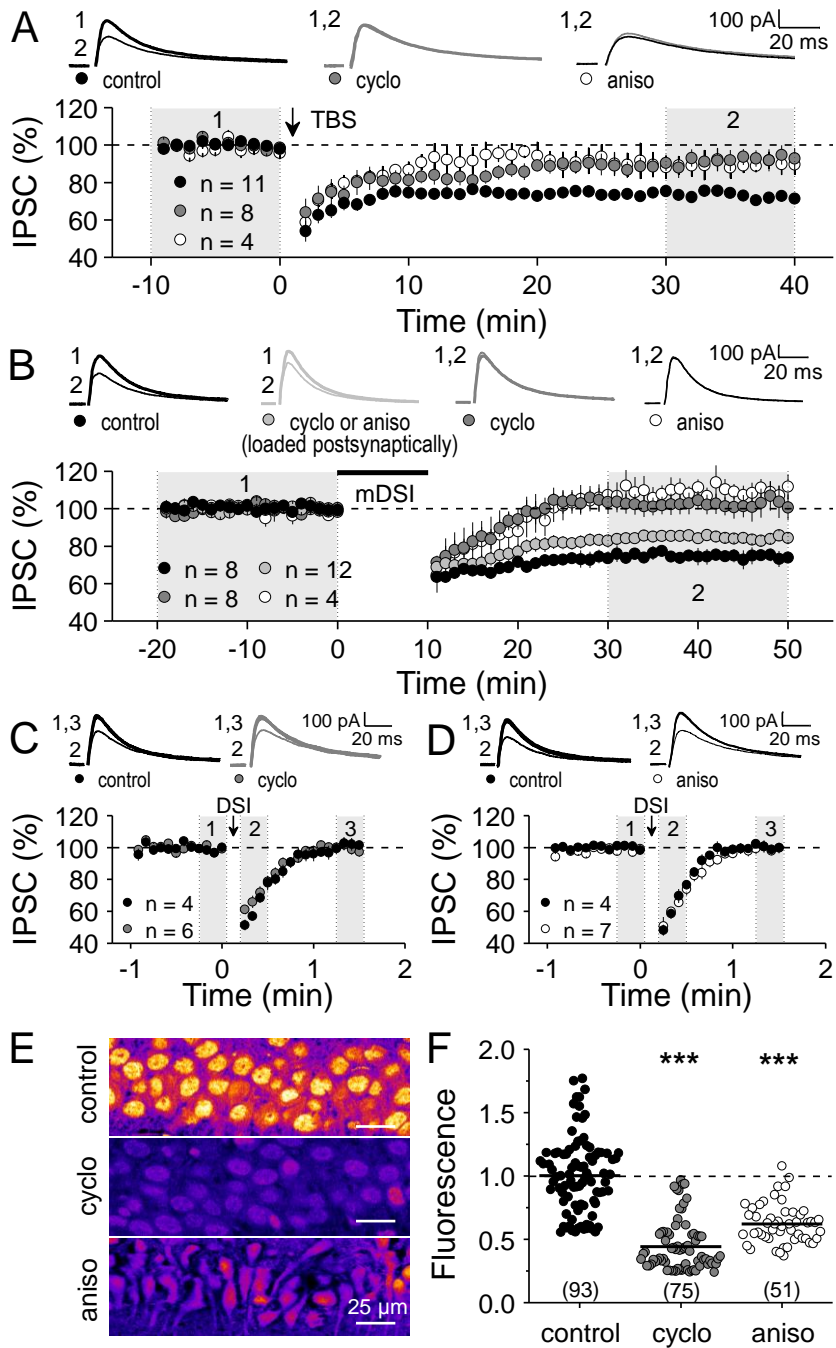
References

- Adermark, L., Talani, G., and Lovinger, D.M. (2009). Endocannabinoid-dependent plasticity at GABAergic and glutamatergic synapses in the striatum is regulated by synaptic activity. *Eur J Neurosci* 29, 32-41.
- Akins, M.R., Leblanc, H.F., Stackpole, E.E., Chyung, E., and Fallon, J.R. (2012). Systematic mapping of fragile X granules in the mouse brain reveals a potential role for presynaptic FMRP in sensorimotor functions. *J Comp Neurol* 520, 3687-3706.
- Alvarez, J., Giuditta, A., and Koenig, E. (2000). Protein synthesis in axons and terminals: significance for maintenance, plasticity and regulation of phenotype. With a critique of slow transport theory. *Prog Neurobiol* 62, 1-62.
- Argaw, A., Duff, G., Zabouri, N., Cecyre, B., Chaine, N., Cherif, H., Tea, N., Lutz, B., Ptito, M., and Bouchard, J.F. (2011). Concerted action of CB1 cannabinoid receptor and deleted in colorectal cancer in axon guidance. *J Neurosci* 31, 1489-1499.
- Baleriola, J., Walker, C.A., Jean, Y.Y., Cray, J.F., Troy, C.M., Nagy, P.L., and Hengst, U. (2014). Axonally synthesized ATF4 transmits a neurodegenerative signal across brain regions. *Cell* 158, 1159-1172.
- Barna, L., Dudok, B., Miczan, V., Horvath, A., Laszlo, Z.I., and Katona, I. (2016). Correlated confocal and super-resolution imaging by VividSTORM. *Nat Protoc* 11, 163-183.
- Barnes, S.J., Opitz, T., Merckens, M., Kelly, T., von der Brélie, C., Krueppel, R., and Beck, H. (2010). Stable mossy fiber long-term potentiation requires calcium influx at the granule cell soma, protein synthesis, and microtubule-dependent axonal transport. *J Neurosci* 30, 12996-13004.
- Basu, J., Srinivas, K.V., Cheung, S.K., Taniguchi, H., Huang, Z.J., and Siegelbaum, S.A. (2013). A cortico-hippocampal learning rule shapes inhibitory microcircuit activity to enhance hippocampal information flow. *Neuron* 79, 1208-1221.
- Beaumont, V., Zhong, N., Fletcher, R., Froemke, R.C., and Zucker, R.S. (2001). Phosphorylation and local presynaptic protein synthesis in calcium- and calcineurin-dependent induction of crayfish long-term facilitation. *Neuron* 32, 489-501.
- Berghuis, P., Rajnicek, A.M., Morozov, Y.M., Ross, R.A., Mulder, J., Urban, G.M., Monory, K., Marsicano, G., Matteoli, M., Canty, A., *et al.* (2007). Hardwiring the brain: endocannabinoids shape neuronal connectivity. *Science* 316, 1212-1216.
- Biro, A.A., Holderith, N.B., and Nusser, Z. (2006). Release probability-dependent scaling of the postsynaptic responses at single hippocampal GABAergic synapses. *J Neurosci* 26, 12487-12496.
- Buffington, S.A., Huang, W., and Costa-Mattioli, M. (2014). Translational control in synaptic plasticity and cognitive dysfunction. *Annu Rev Neurosci* 37, 17-38.
- Cajigas, I.J., Tushev, G., Will, T.J., tom Dieck, S., Fuerst, N., and Schuman, E.M. (2012). The local transcriptome in the synaptic neuropil revealed by deep sequencing and high-resolution imaging. *Neuron* 74, 453-466.
- Calixto, E., Thiels, E., Klann, E., and Barrionuevo, G. (2003). Early maintenance of hippocampal mossy fiber-long-term potentiation depends on protein and RNA synthesis and presynaptic granule cell integrity. *J Neurosci* 23, 4842-4849.
- Castillo, P.E. (2012). Presynaptic LTP and LTD of excitatory and inhibitory synapses. *Cold Spring Harb Perspect Biol* 4.
- Castillo, P.E., Younts, T.J., Chavez, A.E., and Hashimoto, Y. (2012). Endocannabinoid signaling and synaptic function. *Neuron* 76, 70-81.
- Chevaleyre, V., and Castillo, P.E. (2003). Heterosynaptic LTD of hippocampal GABAergic synapses: a novel role of endocannabinoids in regulating excitability. *Neuron* 38, 461-472.
- Chevaleyre, V., Heifets, B.D., Kaeser, P.S., Sudhof, T.C., and Castillo, P.E. (2007). Endocannabinoid-mediated long-term plasticity requires cAMP/PKA signaling and RIM1alpha. *Neuron* 54, 801-812.
- Christie, S.B., Akins, M.R., Schwob, J.E., and Fallon, J.R. (2009). The FXG: a presynaptic fragile X granule expressed in a subset of developing brain circuits. *J Neurosci* 29, 1514-1524.
- Crispino, M., Chun, J.T., Cefaliello, C., Perrone Capano, C., and Giuditta, A. (2014). Local gene expression in nerve endings. *Dev Neurobiol* 74, 279-291.
- Darnell, J.C., and Klann, E. (2013). The translation of translational control by FMRP: therapeutic targets for FXS. *Nat Neurosci* 16, 1530-1536.

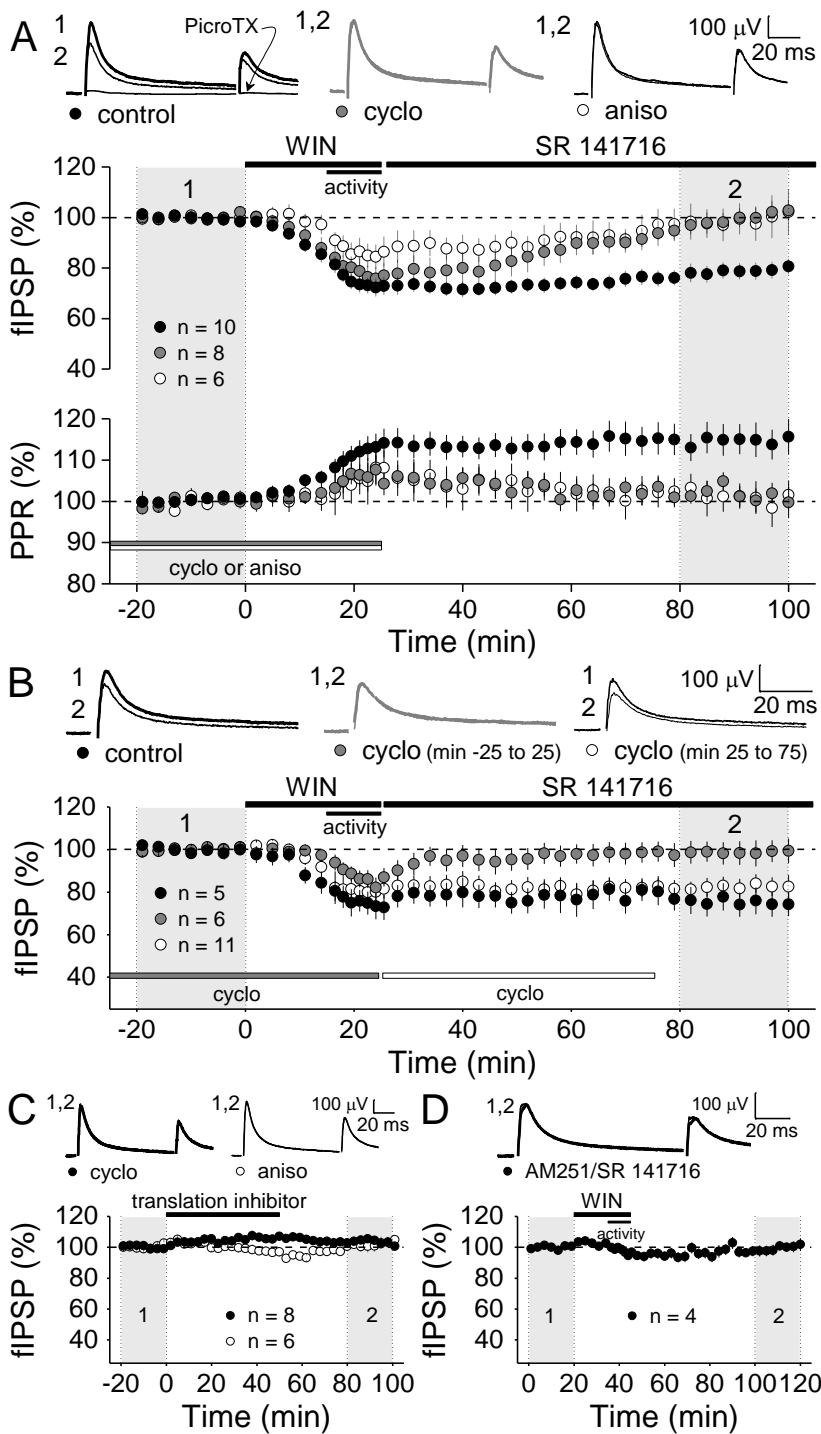
- Dieterich, D.C., Hodas, J.J., Gouzer, G., Shadrin, I.Y., Ngo, J.T., Triller, A., Tirrell, D.A., and Schuman, E.M. (2010). In situ visualization and dynamics of newly synthesized proteins in rat hippocampal neurons. *Nat Neurosci* 13, 897-905.
- Droz, B., and Leblond, C.P. (1963). Axonal Migration of Proteins in the Central Nervous System and Peripheral Nerves as Shown by Radioautography. *J Comp Neurol* 121, 325-346.
- Dudok, B., Barna, L., Ledri, M., Szabo, S.I., Szabadits, E., Pinter, B., Woodhams, S.G., Henstridge, C.M., Balla, G.Y., Nyilas, R., *et al.* (2015). Cell-specific STORM super-resolution imaging reveals nanoscale organization of cannabinoid signaling. *Nat Neurosci* 18, 75-86.
- Dupret, D., O'Neill, J., and Csicsvari, J. (2013). Dynamic reconfiguration of hippocampal interneuron circuits during spatial learning. *Neuron* 78, 166-180.
- Fukudome, Y., Ohno-Shosaku, T., Matsui, M., Omori, Y., Fukaya, M., Tsubokawa, H., Taketo, M.M., Watanabe, M., Manabe, T., and Kano, M. (2004). Two distinct classes of muscarinic action on hippocampal inhibitory synapses: M2-mediated direct suppression and M1/M3-mediated indirect suppression through endocannabinoid signalling. *Eur J Neurosci* 19, 2682-2692.
- Gomes, C., Merianda, T.T., Lee, S.J., Yoo, S., and Twiss, J.L. (2014). Molecular determinants of the axonal mRNA transcriptome. *Dev Neurobiol* 74, 218-232.
- Hagena, H., and Manahan-Vaughan, D. (2013). Differentiation in the protein synthesis-dependency of persistent synaptic plasticity in mossy fiber and associational/commissural CA3 synapses in vivo. *Front Integr Neurosci* 7, 10.
- Heifets, B.D., Chevaleyre, V., and Castillo, P.E. (2008). Interneuron activity controls endocannabinoid-mediated presynaptic plasticity through calcineurin. *Proc Natl Acad Sci U S A* 105, 10250-10255.
- Holt, C.E., and Schuman, E.M. (2013). The central dogma decentralized: new perspectives on RNA function and local translation in neurons. *Neuron* 80, 648-657.
- Howlett, A.C., Barth, F., Bonner, T.I., Cabral, G., Casellas, P., Devane, W.A., Felder, C.C., Herkenham, M., Mackie, K., Martin, B.R., *et al.* (2002). International Union of Pharmacology. XXVII. Classification of cannabinoid receptors. *Pharmacol Rev* 54, 161-202.
- Huang, B., Wang, W., Bates, M., and Zhuang, X. (2008). Three-dimensional super-resolution imaging by stochastic optical reconstruction microscopy. *Science* 319, 810-813.
- Huang, C.C., and Hsu, K.S. (2004). Local protein synthesis and GABAB receptors regulate the reversibility of long-term potentiation at murine hippocampal mossy fibre-CA3 synapses. *J Physiol* 561, 91-108.
- Huang, Y.Y., Li, X.C., and Kandel, E.R. (1994). cAMP contributes to mossy fiber LTP by initiating both a covalently mediated early phase and macromolecular synthesis-dependent late phase. *Cell* 79, 69-79.
- Huber, K.M., Kayser, M.S., and Bear, M.F. (2000). Role for rapid dendritic protein synthesis in hippocampal mGluR-dependent long-term depression. *Science* 288, 1254-1257.
- Irving, A.J., Coutts, A.A., Harvey, J., Rae, M.G., Mackie, K., Bewick, G.S., and Pertwee, R.G. (2000). Functional expression of cell surface cannabinoid CB(1) receptors on presynaptic inhibitory terminals in cultured rat hippocampal neurons. *Neuroscience* 98, 253-262.
- Jones, E.G., and Powell, T.P. (1969). Synapses on the axon hillocks and initial segments of pyramidal cell axons in the cerebral cortex. *J Cell Sci* 5, 495-507.
- Jung, H., Gkogkas, C.G., Sonenberg, N., and Holt, C.E. (2014). Remote control of gene function by local translation. *Cell* 157, 26-40.
- Jung, K.M., Sepers, M., Henstridge, C.M., Lassalle, O., Neuhofer, D., Martin, H., Ginger, M., Frick, A., DiPatrizio, N.V., Mackie, K., *et al.* (2012). Uncoupling of the endocannabinoid signalling complex in a mouse model of fragile X syndrome. *Nat Commun* 3, 1080.
- Kano, M., Ohno-Shosaku, T., Hashimotodani, Y., Uchigashima, M., and Watanabe, M. (2009). Endocannabinoid-mediated control of synaptic transmission. *Physiol Rev* 89, 309-380.
- Katona, I., Sperlagh, B., Sik, A., Kafalvi, A., Vizi, E.S., Mackie, K., and Freund, T.F. (1999). Presynaptically located CB1 cannabinoid receptors regulate GABA release from axon terminals of specific hippocampal interneurons. *J Neurosci* 19, 4544-4558.
- Kelly, A., Mullany, P.M., and Lynch, M.A. (2000). Protein synthesis in entorhinal cortex and long-term potentiation in dentate gyrus. *Hippocampus* 10, 431-437.
- Klausberger, T., Marton, L.F., O'Neill, J., Huck, J.H., Dalezios, Y., Fuentealba, P., Suen, W.Y., Papp, E., Kaneko, T., Watanabe, M., *et al.* (2005). Complementary roles of cholecystokinin- and parvalbumin-expressing GABAergic neurons in hippocampal network oscillations. *J Neurosci* 25, 9782-9793.

- Klein, M.E., Castillo, P.E., and Jordan, B.A. (2015). Coordination between Translation and Degradation Regulates Inducibility of mGluR-LTD. *Cell Rep*.
- Koenig, E., Martin, R., Titmus, M., and Sotelo-Silveira, J.R. (2000). Cryptic peripheral ribosomal domains distributed intermittently along mammalian myelinated axons. *J Neurosci* 20, 8390-8400.
- Martin, K.C., Casadio, A., Zhu, H., Yaping, E., Rose, J.C., Chen, M., Bailey, C.H., and Kandel, E.R. (1997). Synapse-specific, long-term facilitation of aplysia sensory to motor synapses: a function for local protein synthesis in memory storage. *Cell* 91, 927-938.
- Moerke, N.J., Aktas, H., Chen, H., Cantel, S., Reibarkh, M.Y., Fahmy, A., Gross, J.D., Degterev, A., Yuan, J., Chorev, M., *et al.* (2007). Small-molecule inhibition of the interaction between the translation initiation factors eIF4E and eIF4G. *Cell* 128, 257-267.
- Njoo, C., Agarwal, N., Lutz, B., and Kuner, R. (2015). The Cannabinoid Receptor CB1 Interacts with the WAVE1 Complex and Plays a Role in Actin Dynamics and Structural Plasticity in Neurons. *PLoS Biol* 13, e1002286.
- Palay, S.L., and Palade, G.E. (1955). The fine structure of neurons. *J Biophys Biochem Cytol* 1, 69-88.
- Puighermanal, E., Marsicano, G., Busquets-Garcia, A., Lutz, B., Maldonado, R., and Ozaita, A. (2009). Cannabinoid modulation of hippocampal long-term memory is mediated by mTOR signaling. *Nat Neurosci* 12, 1152-1158.
- Roland, A.B., Ricobaraza, A., Carrel, D., Jordan, B.M., Rico, F., Simon, A., Humbert-Claude, M., Ferrier, J., McFadden, M.H., Scheuring, S., *et al.* (2014). Cannabinoid-induced actomyosin contractility shapes neuronal morphology and growth. *Elife* 3, e03159.
- Santini, E., Huynh, T.N., and Klann, E. (2014). Mechanisms of translation control underlying long-lasting synaptic plasticity and the consolidation of long-term memory. *Prog Mol Biol Transl Sci* 122, 131-167.
- Sekine, Y., Zyryanova, A., Crespillo-Casado, A., Fischer, P.M., Harding, H.P., and Ron, D. (2015). Stress responses. Mutations in a translation initiation factor identify the target of a memory-enhancing compound. *Science* 348, 1027-1030.
- Shigeoka, T., Jung, H., Jung, J., Turner-Bridger, B., Ohk, J., Lin, J.Q., Amieux, P.S., and Holt, C.E. (2016). Dynamic Axonal Translation in Developing and Mature Visual Circuits. *Cell* 166, 181-192.
- Sonenberg, N., and Hinnebusch, A.G. (2009). Regulation of translation initiation in eukaryotes: mechanisms and biological targets. *Cell* 136, 731-745.
- Steward, O., and Ribak, C.E. (1986). Polyribosomes associated with synaptic specializations on axon initial segments: localization of protein-synthetic machinery at inhibitory synapses. *J Neurosci* 6, 3079-3085.
- Taylor, A.M., Berchtold, N.C., Perreau, V.M., Tu, C.H., Li Jeon, N., and Cotman, C.W. (2009). Axonal mRNA in uninjured and regenerating cortical mammalian axons. *J Neurosci* 29, 4697-4707.
- Tcherkezian, J., Brittis, P.A., Thomas, F., Roux, P.P., and Flanagan, J.G. (2010). Transmembrane receptor DCC associates with protein synthesis machinery and regulates translation. *Cell* 141, 632-644.
- Twitchell, W., Brown, S., and Mackie, K. (1997). Cannabinoids inhibit N- and P/Q-type calcium channels in cultured rat hippocampal neurons. *J Neurophysiol* 78, 43-50.
- Wilhelm, B.G., Mandad, S., Truckenbrodt, S., Krohnert, K., Schafer, C., Rammner, B., Koo, S.J., Classen, G.A., Krauss, M., Haucke, V., *et al.* (2014). Composition of isolated synaptic boutons reveals the amounts of vesicle trafficking proteins. *Science* 344, 1023-1028.
- Xue, S., and Barna, M. (2012). Specialized ribosomes: a new frontier in gene regulation and organismal biology. *Nat Rev Mol Cell Biol* 13, 355-369.
- Yin, H.H., Davis, M.I., Ronesi, J.A., and Lovinger, D.M. (2006). The role of protein synthesis in striatal long-term depression. *J Neurosci* 26, 11811-11820.
- Yoon, B.C., Jung, H., Dwivedy, A., O'Hare, C.M., Zivraj, K.H., and Holt, C.E. (2012). Local translation of extranuclear lamin B promotes axon maintenance. *Cell* 148, 752-764.
- Younts, T.J., Chevaleyre, V., and Castillo, P.E. (2013). CA1 pyramidal cell theta-burst firing triggers endocannabinoid-mediated long-term depression at both somatic and dendritic inhibitory synapses. *J Neurosci* 33, 13743-13757.
- Yuan, S., and Burrell, B.D. (2013). Endocannabinoid-dependent long-term depression in a nociceptive synapse requires coordinated presynaptic and postsynaptic transcription and translation. *J Neurosci* 33, 4349-4358.

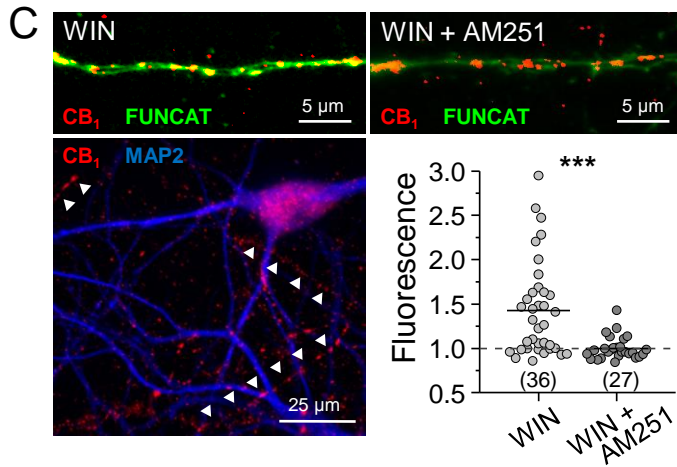
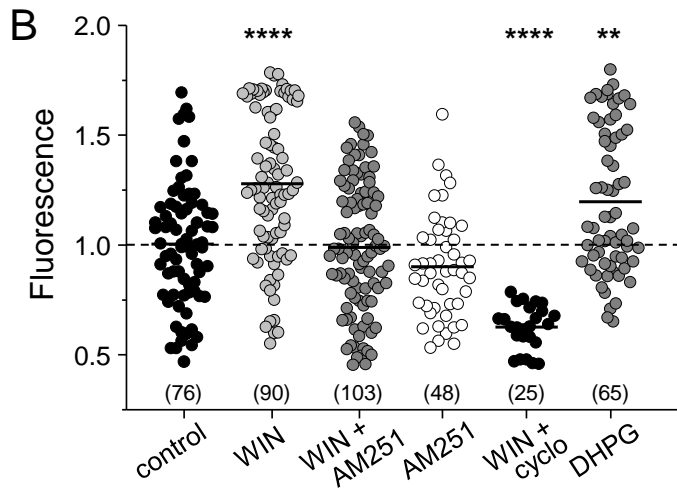
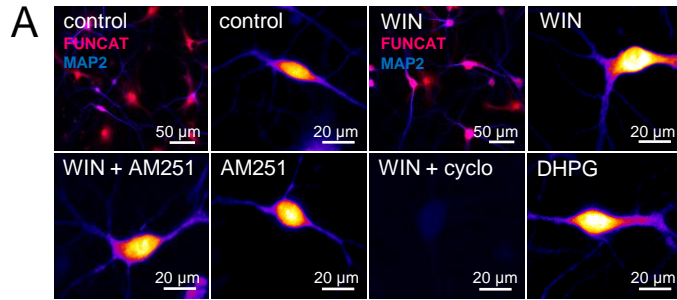
Zhang, X., and Poo, M.M. (2002). Localized synaptic potentiation by BDNF requires local protein synthesis in the developing axon. *Neuron* 36, 675-688.

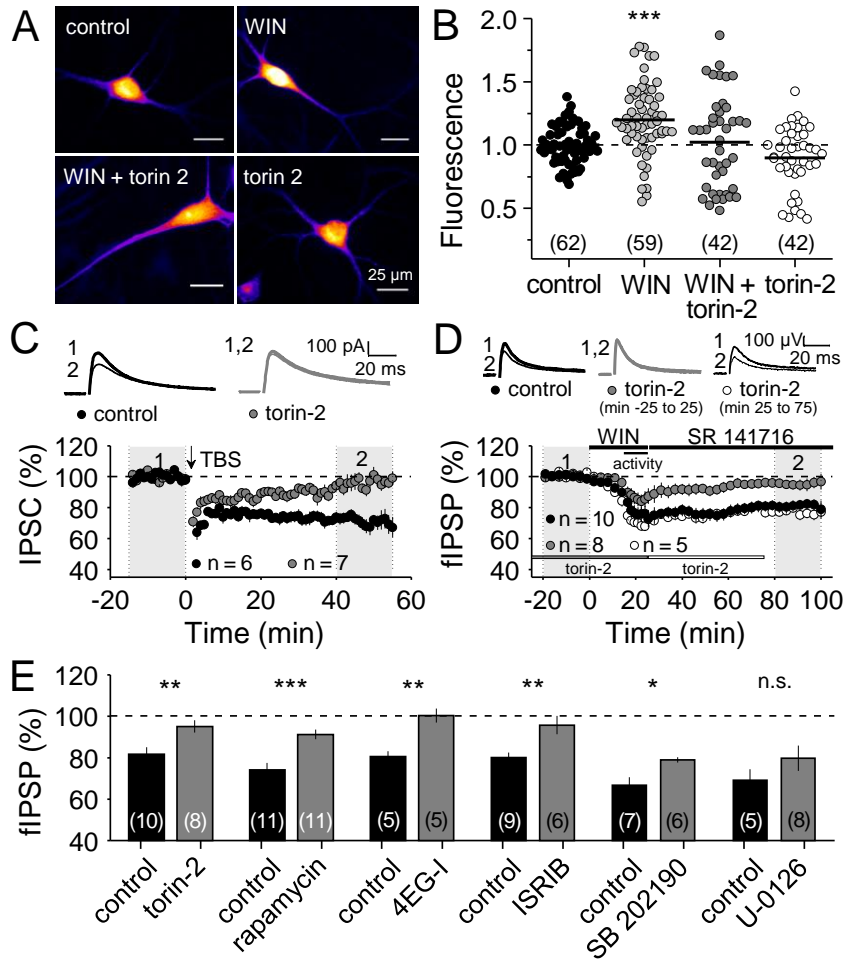


Younts *et al.* Figure 1

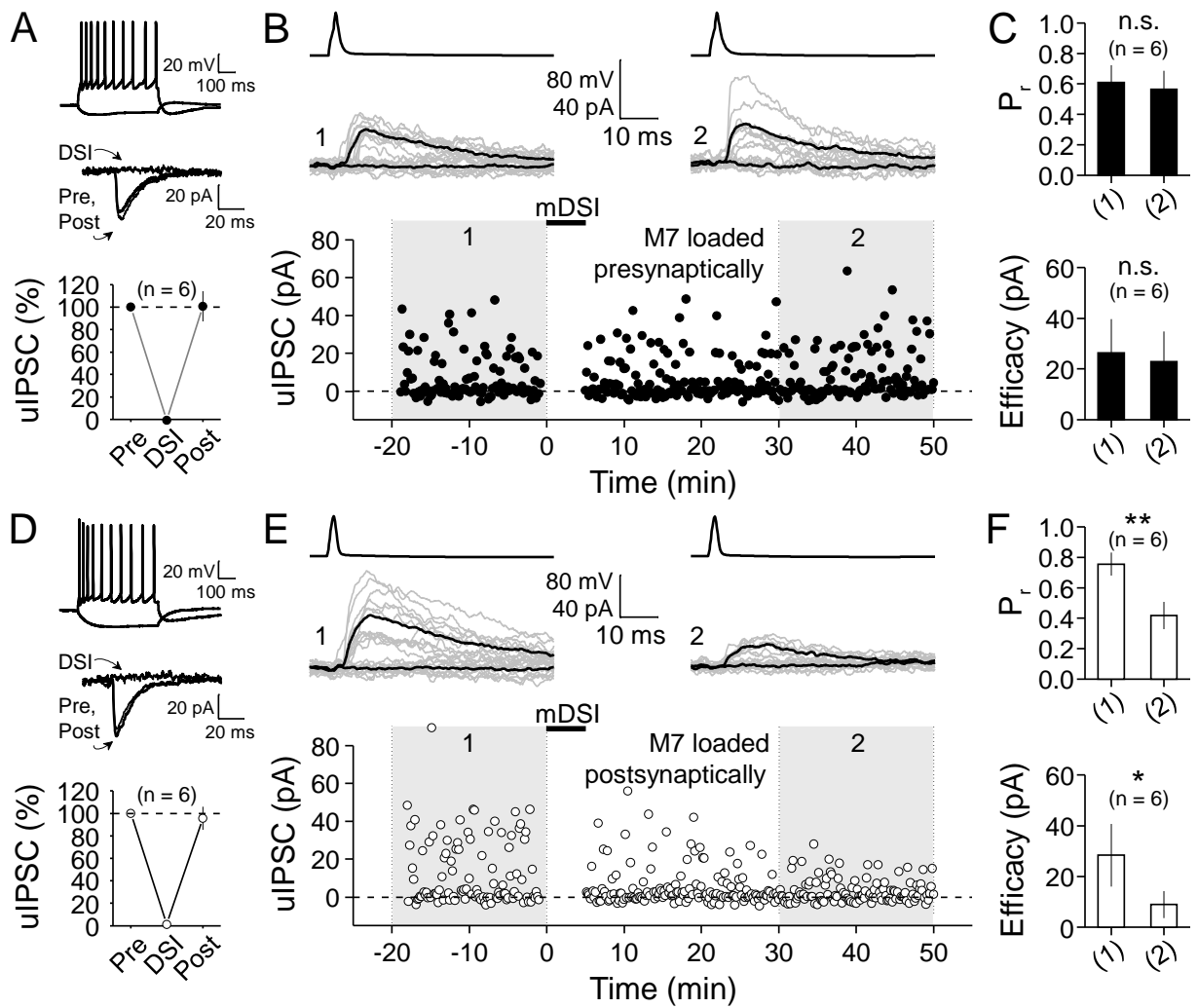


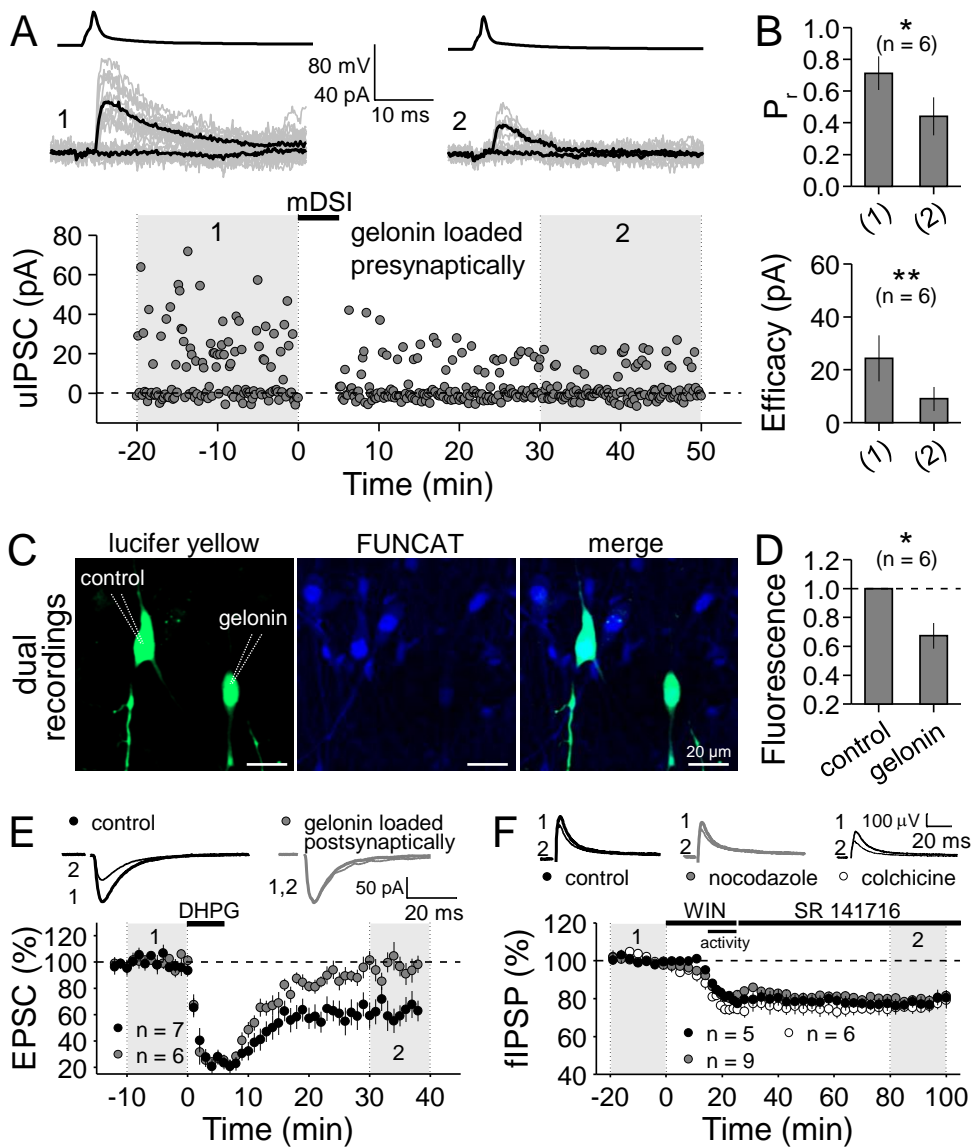
Younts *et al.* Figure 2



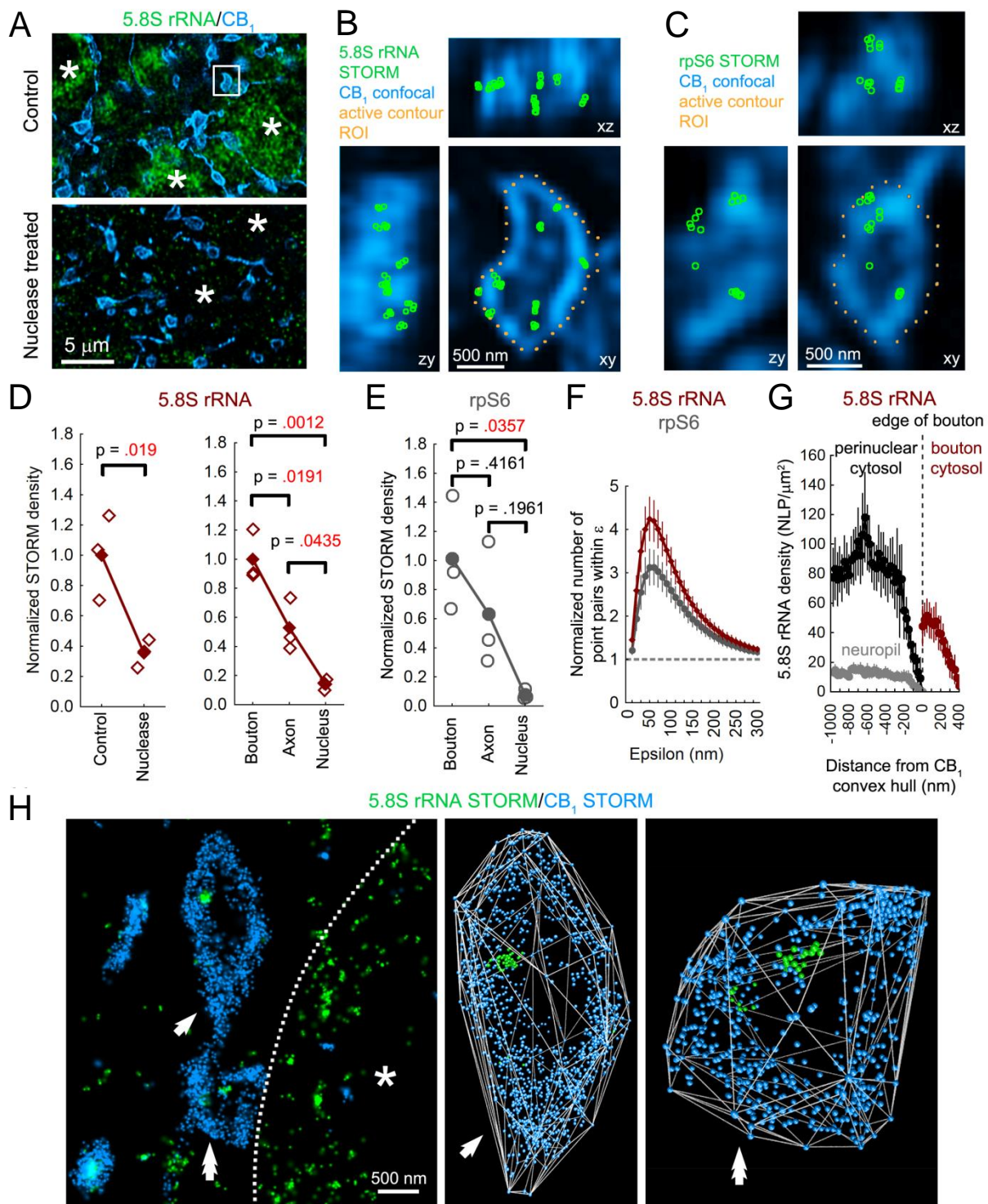


Younts *et al.* Figure 4





Younts *et al.* Figure 6



Younts *et al.* Figure 7

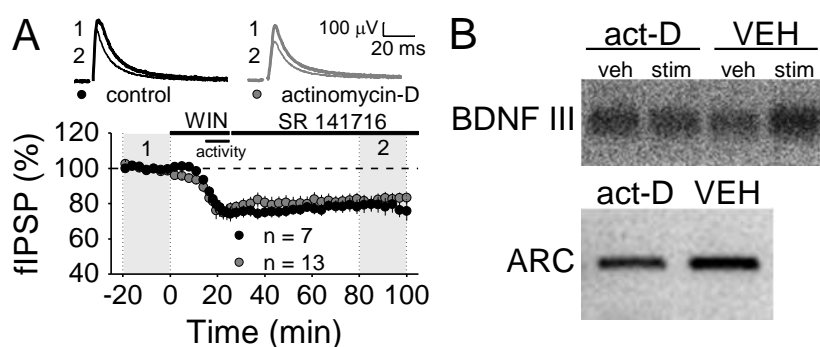


Figure S1 (related to Figure 2): Transcription is not required for iLTD. (A) Transcription inhibitor actinomycin-D (25 μ M) did not affect chemical iLTD. Control: $79.2 \pm 4.6\%$ vs. actinomycin-D: 82.0 ± 3.2 ; $p = 0.60436$, unpaired t-test. Slices pre-incubated in actinomycin-D for >1 hr. Actinomycin-D is irreversible; it was not present during field recordings. Data are shown as mean \pm SEM. (B) To confirm actinomycin-D efficacy (act-D, 25 μ M, slices pre-incubated for 1 hr), BDNF exon III mRNA transcription was measured with RT-PCR on slices stimulated with 60 mM KCl/20 μ M forskolin (Tao et al., 1998). Compared with vehicle (VEH)-treated slices, act-D reduced BDNF exon III transcription (act-D: 0.85-fold decrease vs. vehicle: 1.67-fold increase). We also measured constitutive ARC mRNA transcription. Hippocampal ARC mRNA has a half-life of \sim 1 hr (Rao et al., 2006). Compared with naïve, VEH-treated control, ARC mRNA was reduced (0.75 fold) in slices pretreated for 1 hr with act-D. Band intensity quantified using ImageJ.

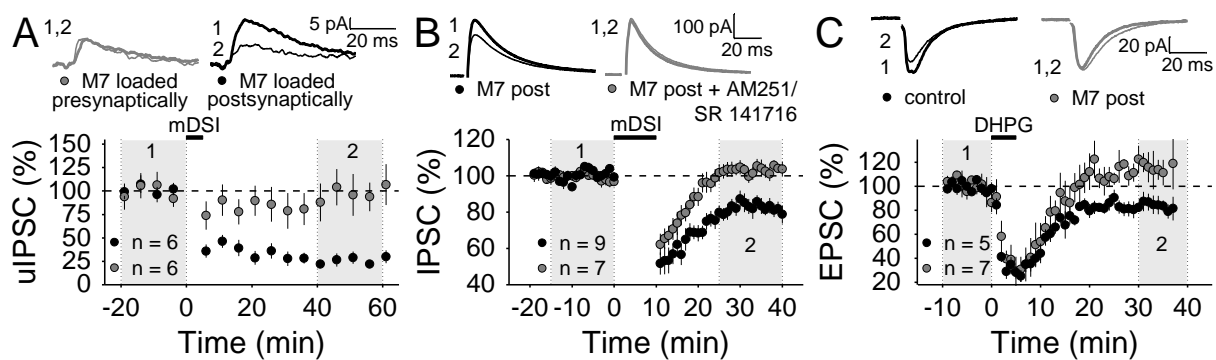


Figure S2 (related to Figure 5): Postsynaptic protein synthesis is dispensable for iLTD. (A) Summary data replotted from paired recording in **Figure 5** to illustrate time-course of averaged uIPSCs (calculated from synaptic efficacy). M7 loaded presynaptically ($89.1 \pm 20.3\%$) vs. M7 loaded postsynaptically ($24.0 \pm 6.2\%$; $p = 0.01482$, paired t-test). Because stochastic transmitter release is more apparent in paired recordings, data were binned every 5 min. Black bar, mDSI protocol. (B) iLTD still relied on CB_1 signaling when M7 ($250 \mu\text{M}$) was loaded postsynaptically into CA1 pyramidal cells. M7 post: $81.9 \pm 3.8\%$ vs. M7 post + AM251 ($4 \mu\text{M}$, $n = 3$) or SR 141716 ($4 \mu\text{M}$, $n = 4$): $102.5 \pm 2.7\%$; $p = 0.00056$, unpaired t-test (AM251 and SR 141716 results pooled because there was no difference). M7 was loaded postsynaptically for 29.5 ± 4.1 min prior to inducing iLTD under control conditions and 27.1 ± 1.5 min in the presence of CB_1 blockers. Slices pre-incubated (> 1 hr) and continuously perfused with AM251 or SR 141716. Black bar, mDSI protocol. (C) Chemically-induced mGluR-LTD (DHPG, $50 \mu\text{M}$, black bar) was blocked by loading M7 ($250 \mu\text{M}$) postsynaptically into CA1 pyramidal cells for 19.9 ± 2.7 min. Control: $83.5 \pm 5.4\%$ vs. M7 post: $114.0 \pm 7.1\%$; $p = 0.00581$, unpaired t-test. Data are shown as mean \pm SEM.

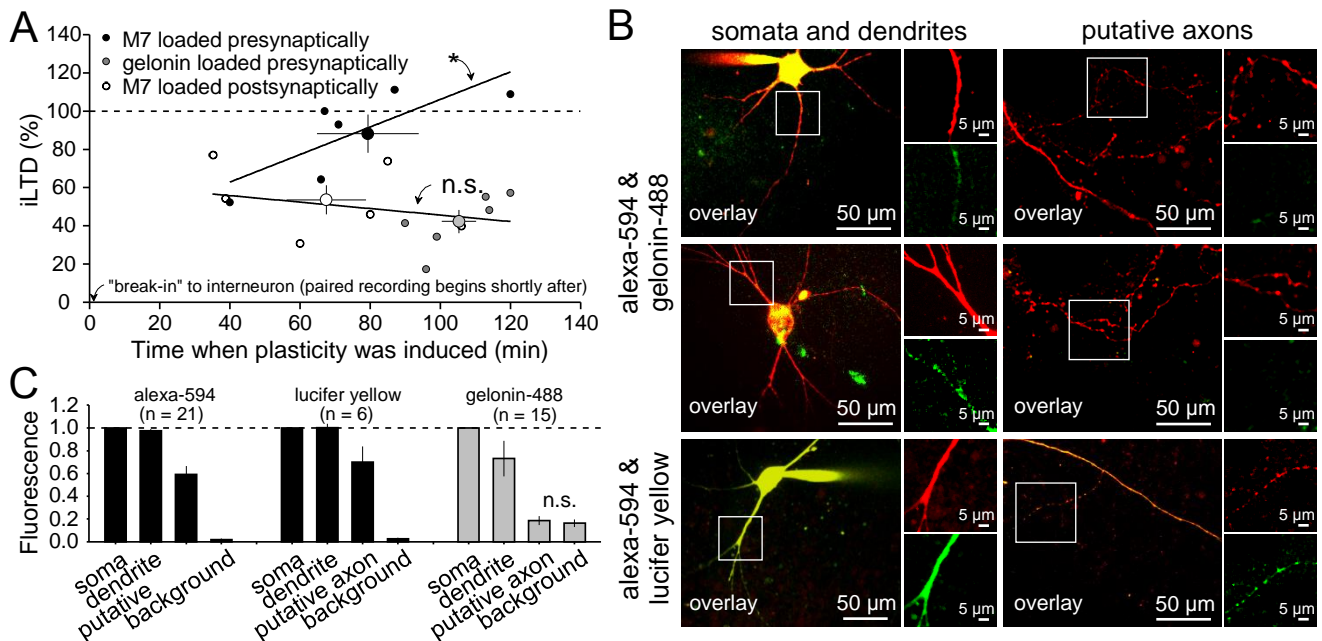


Figure S3 (related to Figures 5 and 6): iLTD likely involves axonal protein synthesis. (A) Magnitude of iLTD (i.e. synaptic efficacy expressed as % of baseline) re-plotted from paired recordings (c.f. Figure 5B,C,E,F and Figure 6A,B) as a function of when iLTD was induced. Consistent with M7 diffusing into remote axonal compartments to exert its blocking effect, the blocking effect of M7 (250 μ M) positively correlated with loading time (Pearson's $r = 0.64687$; $p = 0.04323$). The average time iLTD was induced, and therefore the time interneurons were held in the whole-cell recording configuration prior to inducing iLTD, was not significantly different between M7 loaded presynaptically (79.3 ± 14.5 min) vs. M7 loaded postsynaptically (67.5 ± 11.4 min); $p = 0.53521$, unpaired t-test. Gelonin (3 μ M) was loaded presynaptically for 105.3 ± 4.9 min to block translation in somata/proximal neurites (c.f. Figure 6C,D). Data are shown as mean \pm SEM. (B) M7 proxies, but not gelonin, were detected in CA1 interneuron putative axons in acute hippocampal slices using two-photon fluorescence microscopy. Top two rows: images were collected after loading M7 proxy Alexa Fluor 594 (alex-594, ~760 Da, 250 μ M, shown in red) and fluorescently labeled gelonin-Alexa Fluor 488 (gelonin-488, ~30 kDa, 30 μ M, shown in green) for >100 min in paired recordings (iLTD was observed in these paired recordings, data not shown). Whereas M7 proxy was readily detected in somata, dendrites, and axons, gelonin was detected only in somata and proximal dendrites, not axons. M7 is ~800 Da. Bottom row: interneuron loaded with M7 proxies alexa-594 (250 μ M, shown in red) and Lucifer yellow (~460 Da, 250 μ M, shown in green). Both M7 proxies were detected in somata, dendrites, and putative axons in <1 hr. This experiment also demonstrates that we can detect green fluorescence in axons. Putative axons characterized by their thin width and "beads on a string" appearance. (C) Summary data for panel B. Fluorescence was normalized to the soma for each condition, giving a relative measurement for each fluorophore. Background noise was higher in the gelonin group because we increased the sensitivity of the green fluorescence detector in an effort to detect gelonin. Dendritic measurements (<50 μ m from soma). Putative axon measurements (>250 μ m from soma). $n =$ ROIs imaged per condition for 7 interneurons loaded with alexa-594 (250 μ M), 2 with lucifer yellow (250 μ M), and 5 with gelonin-488 ($n = 2$ with 30 μ M and $n = 3$ with 3 μ M).

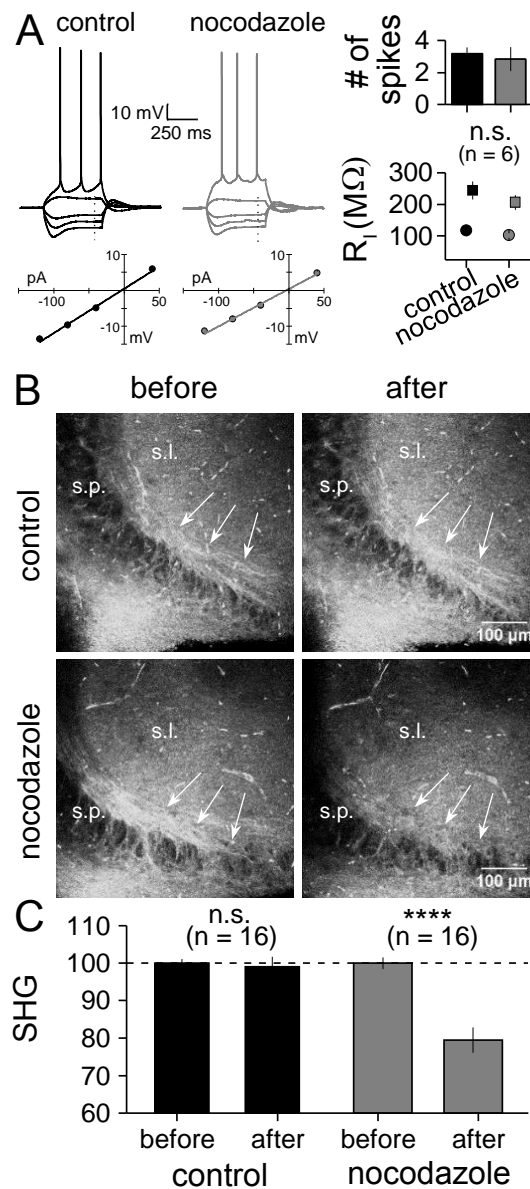


Figure S4 (related to Figure 6): Impact of nocodazole on intrinsic electrophysiological properties and microtubule assemblies. (A) Passive and active intrinsic membrane properties of CA1 neurons in acute hippocampal slices pre-exposed to nocodazole (20 μ M) for 5 and 8 hrs. Top: nocodazole did not significantly change the membrane input resistance (R_i). Voltage deflections collected from pyramidal cells in response to -120, -80, -40, and +40 pA square pulses delivered through the somatic recording pipette. Dashed vertical line indicates measurement of steady-state voltage. Shown below the example sweeps are the averaged steady-state voltage-current relationships for control and nocodazole (n = 3 pyramidal cells each). Slope of the best-fit line was used to calculate R_i . Shown at right is R_i summary data for pyramidal cells (circles) and interneurons (squares). Pyramidal cells: control: $116.9 \pm 6.87 M\Omega$ vs. nocodazole: $102.1 \pm 7.64 M\Omega$; $p = 0.22402$, unpaired t-test. Interneurons: control: $244.2 \pm 28.3 M\Omega$ vs. nocodazole: $206.2 \pm 23.7 M\Omega$; $p = 0.36086$, unpaired t-test). As expected, R_i was higher for interneurons. Also shown are: firing properties (number of spikes in response to +80 pA square pulse). Control: 3.2 ± 0.4 vs. nocodazole: 2.8 ± 0.7 ; $p = 0.70$, unpaired t-test (results pooled across pyramidal cells interneurons because there was no difference). (B) Microtubule stability assessed with second harmonic generation (SHG) microscopy. Microtubules can produce intrinsic optical signals (i.e. SHG) in response to two-photon laser-induced excitation (Dombeck et al., 2003). Representative images show microtubule bundles in hippocampal CA3 mossy fiber axons (white arrows) in acute slices. Compared with control, acute nocodazole (25 μ M) treatment disrupted microtubule assemblies. Before (time 0) and after (time 60). s.l., *stratum lucidum*. s.p. *stratum pyramidal*. (C) Summary data of randomly selected ROIs (n = 16 each) from mossy fiber axons in *s. lucidum*. Control: $99.127 \pm 2.7\%$ of baseline; $p = 0.8209$; nocodazole: $79.5 \pm 3.3\%$ of baseline; $p < 0.0001$, Wilcoxon matched-pairs signed rank test, n = 3 slices each. Data are shown as mean \pm SEM.

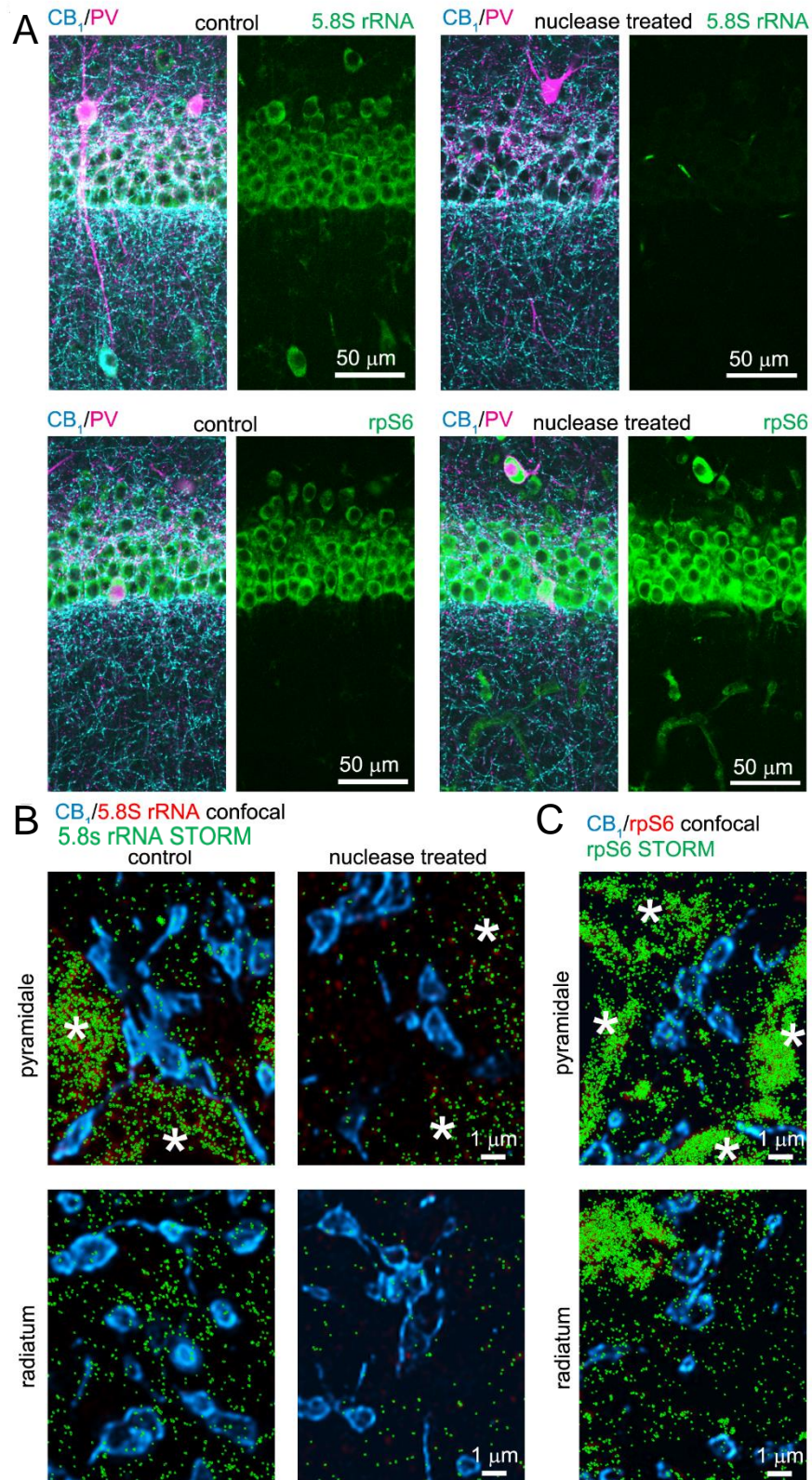


Figure S5 (related to Figure 7): Immunostaining against ribosomal markers in hippocampal CA1. (A) Low-magnification (20x) confocal images of CB₁ and parvalbumin (PV) staining together with 5.8S rRNA or rpS6. As expected, pretreatment of sections with nucleases diminished 5.8S rRNA, but not rpS6 labeling. **(B)** High-magnification (100x) correlated confocal and STORM image of CB₁ and 5.8S rRNA immunostaining shows ribosomal labeling in CB₁-expressing axon terminals across the somatic (*s. pyramidale*) and dendritic (*s. radiatum*) fields. Nuclease treatment substantially reduced 5.8S rRNA labeling. Cell bodies indicated with asterisks. **(C)** Similar to panel B, but for rpS6.

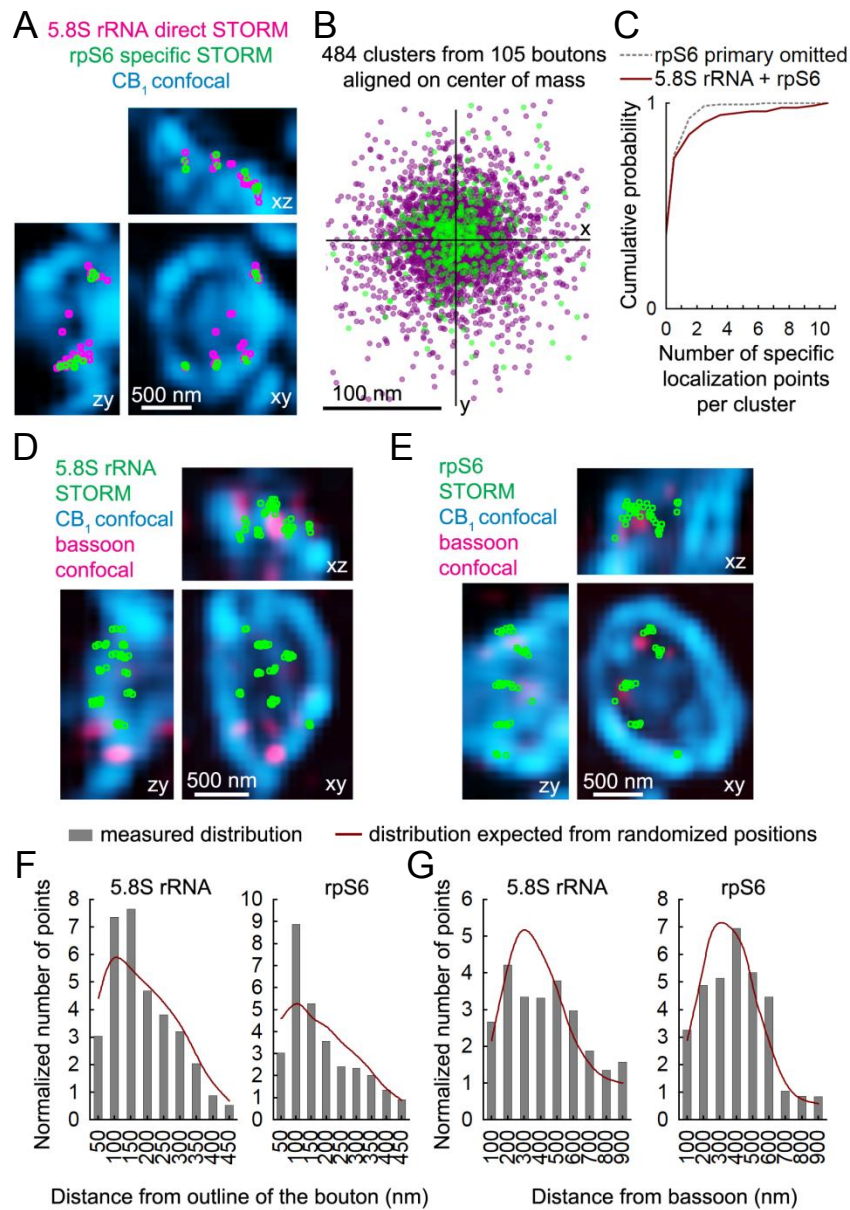


Figure S6 (related to Figure 7): Nanoscale distribution of 5.8S rRNA and rpS6 labeling inside CB1-expressing interneuron axon terminals. (A) “Direct STORM” images of 5.8S rRNA were obtained with a commercially available secondary antibody labeled with AlexaFluor-647 (activated directly with 405 nm light). “Specific STORM” images of rpS6 were obtained with an in-house secondary antibody labeled with Cy3/AlexaFluor-647 (activated specifically with 561 nm light). Note that clusters of localization points in CB₁-expressing axon terminals contain a mixture of points from both channels (see panel E), strongly suggesting the STORM signal originates from the same ribosomal material. As expected, due to the inferior sensitivity of the specific channel, the number of localization points from the specific channel is lower than the direct channel. (B) Scatterplot of the x and y coordinates of localization points after aligning all clusters on their center of mass. Localization points from both channels are distributed around the origin. (C) Cumulative probability distributions of the number of specific localization points (rpS6 labeling) for clusters containing 5.8S rRNA (n = 484 clusters, 103 boutons, 2 animals) and negative controls where the primary antibody against rpS6 was omitted (n = 533 clusters, 105 boutons, 2 animals). A higher number of specific localization points was observed in the presence of the rpS6 antibody, indicating that 5.8S rRNA and rpS6 are co-clustered in CB₁-expressing axon terminals. (D) Correlated confocal and STORM images of a CB₁-positive axon terminal co-expressing the presynaptic active zone protein bassoon and 5.8S rRNA. Multiple bassoon puncta and multiple ribosomal clusters are present in the bouton. (E) Similar to panel A, but for rpS6. (F) Histograms showing the distribution of ribosomal material in axon terminals defined by CB₁ (n = 101 and 125 terminals for 5.8s rRNA and rpS6, respectively, from 3 animals each). STORM localization points 100-150 nm from the inside of the CB₁ label is greater than expected from a random distribution, consistent with the CB₁-5.8S rRNA dual STORM data (c.f. Figure 7G). (G) In the same terminals, the distribution of localization points near bassoon puncta does not significantly differ from a random distribution, suggesting ribosomes are not orderly arranged around the active zone.

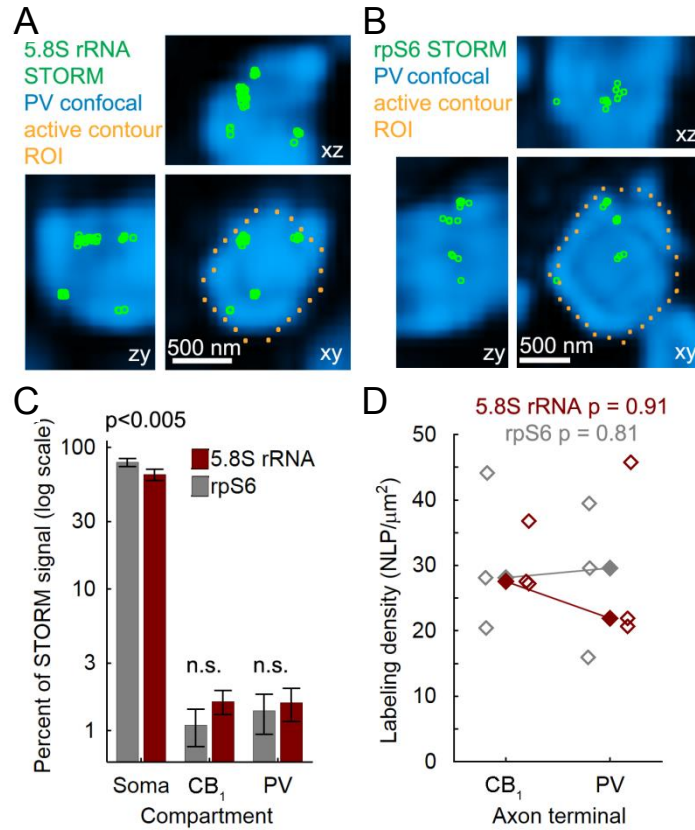


Figure S7 (related to Figure 7): Ribosomal material in parvalbumin (PV)-expressing axon terminals and comparison with CB₁-expressing axon terminals. (A) Correlated confocal and STORM microscopy reveals 5.8S rRNA immunolabeling in PV-expressing axon terminals of basket cells. In contrast to CB₁ labelling, which delimits the terminal, PV is expressed within the terminal. (B) Similar to panel A, but for rpS6. (C) Compartmental distribution of the total ribosomal signal in CB₁ and PV terminals. The distribution of both ribosomal markers within compartments is similar. Summary data shows mean \pm 2x SEM from 28 and 30 images of 5.8S rRNA and rpS6 staining, respectively, from 3 animals, two-sample Kolmogorov-Smirnov test. Analysis performed on images collected at the border between *s. pyramidale* and *radiatum*. (D) Comparison of ribosomal labeling density between CB₁- and PV-expressing axon terminals showing medians (filled diamonds) and individual data points (open diamonds) from 3 animals per group (n = 279 axon terminals were analyzed), unpaired t-test. NLP, number of localization points.

Supplemental Experimental Procedures

Acute hippocampal slices

Experimental procedures adhered to NIH and Albert Einstein College of Medicine Institutional Animal Care and Use Committee guidelines. Acute transverse slices were prepared from young adult male and female Sprague Dawley rats and C57BL/6 mice (P15-30). The cutting solution contained (in mM): 215 sucrose, 20 glucose, 26 NaHCO₃, 4 MgCl₂, 4 MgSO₄, 1.6 NaH₂PO₄, 2.5 KCl, and 1 CaCl₂. The artificial cerebral spinal fluid (ACSF) recording solution contained (in mM): 124 NaCl, 26 NaHCO₃, 10 glucose, 2.5 KCl, 1 NaH₂PO₄, 2.5 CaCl₂, and 1.3 MgSO₄. After ice-cold cutting, slices recovered at 34°C (in 50% cutting solution, 50% ACSF) for <30 min and then at room temperature (RT) for >1 hr in ACSF. All solutions were bubbled with 95% O₂ and 5% CO₂ for at least 30 min. Although the form of long-term inhibitory synaptic plasticity studied here (i.e. iLTD) is present under physiological recording conditions at 37 °C (Younts et al., 2013), inhibitory synaptic transmission is less stable at this temperature, making long-term measurements of inhibition (up to 5 hrs in the present study) not practical. We therefore conducted our experiments at 25.5 ± 0.1°C.

Electrophysiology

For whole-cell recordings, CA1 pyramidal cells were blind patched (>100 µm below slice surface) using an upright Nikon Eclipse E600FN infrared differential interference contrast microscope (4x and 40x plan fluor objectives, NA = 0.13 and 0.8, respectively) equipped with a Cohu monochrome CCD camera and voltage-clamped at -60 mV with an intracellular recording solution containing (in mM): 135 KMeSO₄, 5 KCl, 1 CaCl₂, 5 EGTA, 5 NaOH, 10 HEPES, and 10 glucose; pH 7.2 (280-290 mOsm). IPSCs or EPSCs were pharmacologically isolated with 5 µM NBQX/25 µM D-APV or 100 µM picrotoxin to block AMPA/kainate/NMDA or GABA_A receptors, respectively. Dendritically originating IPSCs/EPSCs and somatically originating IPSCs were evoked with ACSF-filled extracellular stimulating patch-type pipettes (~10 µm broken tip) placed in *stratum (s.) radiatum* or *s. pyramidale* (<10 µA, 200 µs), respectively (~150-200 µm from the recording pipette). For extracellular field IPSP (fIPSP) recordings, the stimulating pipette (filled with ACSF) and recording pipette (filled with 1 M NaCl) were placed in *s. pyramidale* (>100 µm below slice surface, ~150-200 µm apart).

Long-term cell-paired recordings

For paired recordings, interneurons with their soma in *s. radiatum* (typically >100 µm below slice surface and <200 µm from *s. pyramidale*) were visually identified, patched, and their firing pattern characterized in response to 500 ms, 80-240 pA somatic square-wave current pulses as described (Younts et al., 2013). Regular-spiking interneurons often show DSI-sensitivity and therefore express CB₁ (Glickfeld and Scanziani, 2006; Pawelzik et al., 2002). CA1 pyramidal cells residing in *s. pyramidale* (at approximately the same depth in slice) were blind-patched with an intracellular recording solution containing (in mM): 54.5 CsMeSO₄, 60 KCl, 1 CaCl₂, 5 EGTA, 2 NaOH, 10 HEPES, and 10 glucose (measured Cl⁻_{reversal} ~ -20 mV). Interneuron action potentials were evoked in current-clamp mode by a 2 ms, 3-5 nA depolarizing square wave pulse. Action potential-evoked unitary IPSCs (uIPSCs) were recorded from CA1 pyramidal cells in the voltage-clamp mode. Connection probability was ~10%. Only regular-spiking, DSI-sensitive (>50% suppression from baseline) connections were analyzed for iLTD experiments. DSI was induced by a 5 s voltage step (-60 to 0 mV) in the pyramidal cell and quantified by averaging 4-7 sweeps before, after, and recovery from DSI. During the iLTD portion of the experiment, pairs of action potentials (100 ms inter-stimulus interval) were used to evoke uIPSCs (except for two interleaved recordings using a 5 ms inter-stimulus interval).

For all paired recordings, action-potential-evoked uIPSCs (i.e. synaptic responses) were clearly resolvable from non-responses (i.e. synaptic failures). Postsynaptic uIPSCs were classified as responses only if: (a) their latency (2.67 ± 0.13 ms for all connections, range 1.5 – 4.1 ms, n = 18) was precisely time-locked to the presynaptic action potential; and (b) their peak amplitude was >2.3 pA (i.e. the smallest resolvable synaptic responses, which were at least 5 standard deviations greater than the root mean square noise across recordings calculated during the baseline; mean ± standard deviation root mean square noise: 0.71 ± 0.1 pA, range 0.55 – 0.91 pA, n = 18). Average baseline uIPSC peak amplitudes across all paired recordings was 33.4 ± 6.0 pA (range 9.0 – 90.5 pA, n = 18). For quantification, the smallest resolvable uIPSC for each connection was identified and used to classify sweeps as responses or failures. We calculated the following quantal parameters during the baseline and after inducing iLTD (the same number of sweeps, typically 120, were analyzed for each): release probability (estimated as inverse failure rate); synaptic efficacy (average of all action potential-evoked postsynaptic responses and failures); and synaptic potency (average of just synaptic responses). Root mean square noise was not subtracted from quantal parameters. Importantly, the action potential-evoked uIPSC latencies across all experimental conditions (calculated from synaptic efficacy during the baseline) were not significantly different (M7 loaded presynaptically: 2.91 ± 0.24 ms vs. gelonin loaded presynaptically: 2.43 ± 0.23 ms vs. M7 loaded postsynaptically: 2.67 ± 0.19 ms. F[2,15] = 1.18032; p = 0.33415, one-way ANOVA). There also was no difference between the average baseline release probability, synaptic efficacy, and synaptic potency across each condition (cf. **Figure 5C,F** and **Figure 6B**). These analyses indicate that the sampled synaptic connections were not biased towards somatic or dendritic inhibitory inputs. To improve the likelihood of maintaining stable, long-term recordings (average

paired recording duration: 140.7 ± 13.5 min, range: 90-300 min, $n = 18$), pyramidal cells were voltage-clamped (after testing for DSI at -60 mV) at positive potentials (0-30 mV), which facilitated series/access resistance (R_s) stability.

For synaptically-induced iLTD, an at least 20 min baseline was acquired and then the pyramidal cell was returned to -60 mV. The iLTD induction protocol (see below) was administered at -60 mV. During the induction, interneurons were slightly depolarized (via somatic current injection) to yield action potentials at 1-3 Hz because we previously demonstrated that iLTD requires both spontaneous presynaptic activity and CB_1 activation (Heifets et al., 2008). After the induction, the pyramidal cell was returned to the pre-induction holding potential (i.e. 0-30 mV). iLTD was typically quantified 30-50 min post induction, but for two recordings it was 15-35 min because one of the two cells became compromised (we considered this time valid because iLTD manifests immediately after the induction). To measure cell health and stability, interneuron resting membrane potential (V_{rest}) and input resistance (R_i), as well as pyramidal cell R_s and R_i were monitored (with 5 mV hyperpolarizing square wave pulses). If either of the cells became compromised before eliciting iLTD, the experiment was rejected; if either became compromised after eliciting iLTD, the analysis was curtailed at that time (see above). For M7 loaded presynaptically experiments ($n = 6$): V_{rest} for interneurons was -62.9 ± 1.9 mV during baseline and -62.2 ± 2.3 mV after iLTD induction, and R_i for interneurons was 275.4 ± 42.0 M Ω during baseline and 187.7 ± 19.5 M Ω after iLTD induction; R_s for pyramidal cells was 11.5 ± 0.9 M Ω during baseline and 11.9 ± 1.2 M Ω after iLTD induction, and R_i for pyramidal cells was 116.7 ± 14.9 M Ω during baseline and 149.2 ± 22.1 M Ω after iLTD induction. For gelonin loaded presynaptically experiments ($n = 6$, but two interneurons were excluded from this analysis, see below): V_{rest} for interneurons was -60.7 ± 1.4 mV during baseline and -62.3 ± 0.7 mV after iLTD induction, and R_i for interneurons was 208.8 ± 12.7 M Ω during baseline and 181.5 ± 21.2 M Ω after iLTD induction; R_s for pyramidal cells was 14.3 ± 1.9 M Ω during baseline and 13.8 ± 1.7 M Ω after iLTD induction, and R_i for pyramidal cells was 130.9 ± 10.4 M Ω during baseline and 119.2 ± 9.1 M Ω after iLTD induction. For M7 loaded postsynaptically experiments ($n = 6$): V_{rest} for interneurons was -62.1 ± 1.8 mV during baseline and -61.9 ± 1.8 mV after iLTD induction, and R_i for interneurons was 231.5 ± 51.5 M Ω during baseline and 211.2 ± 50.2 M Ω after iLTD induction; R_s for pyramidal cells was 11.9 ± 1.5 M Ω during baseline and 12.6 ± 1.3 M Ω after iLTD induction, and R_i for pyramidal cells was 116.2 ± 19.7 M Ω during baseline and 133.2 ± 28.4 M Ω after iLTD induction ($p > 0.10$ for each, paired t-tests). Notably, there were no differences between conditions in baseline V_{rest} or R_i for interneurons and R_s or R_i for pyramidal cells. These analyses indicate our recordings were stable, and that protein synthesis inhibitors do not significantly alter intrinsic membrane properties.

For experiments employing gelonin, the recording pipette tips were first front-filled with K^+ -based intracellular recording solution lacking gelonin and then back-filled with the same K^+ -based recording solution containing 3.1 μ M gelonin. The estimated final concentration of gelonin was 3 μ M. For two paired recordings in which gelonin was loaded presynaptically for >60 min in the whole-cell configuration, the cell-attached configuration was used to elicit action potentials during the iLTD portion of the experiment.

Long-term plasticity induction protocols

Synaptically-induced iLTD (Chevalyere and Castillo, 2003) was triggered with a theta-burst stimulation (TBS) protocol delivered via an extracellular patch-type pipette placed in *s. radiatum* (**Figure 1A**). TBS consisted of 5 stimuli (i.e. a burst at 100 Hz) delivered 10 times at 5 Hz. This was repeated five times, once every 5 s. We previously demonstrated that postsynaptic activity that mimics CA1 pyramidal cell firing *in vivo* also elicits iLTD (Younts et al., 2013). For the present study, postsynaptically-induced iLTD was triggered by multiple episodes of DSI (mDSI). This protocol engages iLTD at somatic and dendritic inhibitory inputs. For data presented in **Figure 1B** and **Figure S2B**, the iLTD induction protocol consisted of 5 s voltage steps from -60 to 0 mV every 15 s for 10 min; for paired-recordings presented in **Figure 5B,C,E,F** and **Figure 6A,B**, the iLTD induction protocol consisted of 2 s voltage steps from -60 to 0 mV every 5 s for 5 min. To elicit chemical-iLTD (Heifets et al., 2008) in **Figure 2A,B,D**, **Figure 4D,E** and **Figure 6F**, the CB_1 agonist WIN 55,212-2 (WIN; 5 μ M) was bath applied for 25 min, and 5 stimuli at 10 Hz were delivered at 0.1 Hz during the last 10 min of WIN. WIN was chased with the CB_1 inverse agonist/antagonist SR 141716 (5 μ M) or AM251 (5 μ M) to halt CB_1 signaling. To elicit chemical mGluR-LTD in **Figure 6E** and **Figure S2C**, 50 μ M DHPG was bath applied for 5 min.

Electrophysiology data acquisition and statistics

Baseline and post-induction synaptic responses were monitored at 0.05 Hz during iLTD and 0.2 Hz during DSI. Stimulation and acquisition were controlled with IgorPro 5 (Wavemetrics). Shaded boxes in figures correspond to when plasticity was analyzed with respect to baseline and when representative traces were collected and averaged. Summary data (i.e. time-course plots and bar graphs) are presented as mean \pm standard error of mean (SEM). Whole-cell and field recording summary data were respectively binned every 1 and 3 min, unless otherwise indicated. Analysis and statistics were carried out in OriginPro 7.0 and 9.1 (OriginLab). Significance ($p < 0.05$) was assessed with one-way ANOVA (means comparison with *post hoc* Bonferroni test for electrophysiology and FUNCAT or Tukey test for STORM), Student's paired and unpaired t-tests, Wilcoxon matched-pairs signed rank test, Mann Whitney U test, or Pearson's correlation coefficient, as indicated. All experiments were performed in an interleaved fashion. Unless stated otherwise, "n" represents number of independent cells or field recordings in slices.

Electrophysiology reagents

Stock reagents were prepared according to the manufacturer's recommendation in water, DMSO (<0.01% final volume during experiments), or phosphate buffered saline (PBS), stored at -20°C, and diluted into ACSF or intracellular recording solutions as needed. NBQX, D-APV, SR 141716, and WIN were acquired from the NIMH Chemical Synthesis and Drug Supply Program; m⁷GpppG (M7) from New England BioLabs; gelonin from Enzo Life Sciences; 4EGI-1 from EMD Chemicals; cycloheximide, anisomycin, picrotoxin, ISRIB, actinomycin-D, and salts for making cutting, ACSF, and intracellular recording solutions from Sigma-Aldrich; DHPG, AM251, nocodazole, rapamycin, U-0126, U-0124, and SB 202190 from Tocris; colchicine and torin-2 from Cayman Chemical; Lucifer yellow CH (lithium salt), Alexa Fluor-594, and Alexa Fluor-488 protein labeling kit from ThermoFisher Scientific. Reagents were either acutely bath applied, diluted into the intracellular recording solution, or preincubated with slices, as indicated in Results.

Fluorescent noncanonical amino acid tagging (FUNCAT) in hippocampal cultures and slices

Primary hippocampal neurons were prepared from E18-19 rat brains and grown (12-18 days) on poly-D-lysine coated coverslips in Neurobasal media with Glutamax and B-27 supplement (Invitrogen). Neurons were seeded at a density of 65,000 cells/well in a 12-well plate. Neuron cultures grown for 18 days *in vitro* were washed once with PBS (0.01 M, pH = 7.4) and pre-incubated with methionine-free DMEM (Invitrogen) for 30 min to deplete methionine stores. They were then incubated for 1.5 hrs with 100 μM azidohomoalanine (AHA) (Iris Biotechnology, Germany) and treated with reagents, as described in Results, in methionine-free DMEM at 37°C. Neurons were then fixed in 4% paraformaldehyde (PFA), permeabilized with Triton-X 100 and incubated with Click-it® reaction buffer containing 2 μM Alexa Fluor-488 alkyne (Invitrogen) for 30 min at RT. Following the click reaction, samples were blocked for 1 hr at RT in blocking solution (4% (wt/vol) bovine serum albumin, BSA, in PBS), and immunocytochemistry was performed according to standard procedures using chicken anti-microtubule associated protein (MAP2) at 1:500 (EnCor Biotechnology Inc., 7225-4) to specifically label neuronal dendrites.

Images were obtained on a Zeiss Axio-Observer inverted microscope (20x and 63x plan apochromat objectives, NA = 0.8 and 1.4, respectively) equipped with an AxioCam Mrm (12-bit resolution) camera using the same settings for all samples within an experiment. Experimenter was blind to the treatment condition during imaging and analysis. Image analysis was performed with ImageJ (NIH). For **Figure 4A**, images were acquired at 20x and MAP2 staining, which exclusively labels microtubules in neurons, was used to randomly select neurons for image analysis. Thus, translation was assayed only in neurons, not astrocytes or other cells. Thresholded MAP2 signal was used to generate a region of interest (ROI) for an image. In this case, the ROIs included somata and dendrites of all (i.e. 2-8) neurons in a single image (~5 images/condition). The mean FUNCAT fluorescence intensity was calculated to give a single value/image. For **Figure 4C**, images of neurons were acquired at 63x to resolve CB₁ immunostaining. To assess FUNCAT signal underneath CB₁ puncta and putative axons, a thresholded MAP2 mask was applied to the CB₁ channel. CB₁ labeling that fell within the MAP2 mask was cleared. The remaining CB₁ labeling was thresholded to generate a second mask that was applied to the FUNCAT channel. Values reported are the mean fluorescence (i.e. pixel intensity, or gray value) of all regions of interest (ROI) in the image normalized to the mean fluorescence of all ROIs in the control group. For image presentation, the background was subtracted and the image cropped.

We carried out FUNCAT on acute hippocampal slices using a previously published protocol (Tom Dieck et al., 2012). For experiments in **Figure 1E,F**, slices were incubated in AHA (1 mM) in the presence of cycloheximide, anisomycin, or DMSO (control) in oxygenated ACSF. After 2.5 hrs, slices were fixed overnight in 4% PFA and 5% sucrose PBS. The following day, slices were embedded in agar and resectioned to 35 μm. Slices were permeabilized and blocked for >2 hrs at RT. Click-it® reaction was performed using 1 μM Alexa Fluor-647 (ThermoFisher Scientific) for 48 hrs at RT. Slices were washed and mounted before imaging on a Zeiss LSM 510 Meta Duo V2 confocal microscope (63x plan apochromat objective, NA = 1.4) using the same settings for all samples within an experiment. Experimenter was blind to the treatment condition during imaging and analysis. Single plane images (63x) were randomly collected (from the middle of each slice, ~17 μm deep). ImageJ was used to quantify fluorescence, as described above, by generating a circular ROI within neuronal somata located in the CA1 cell body layer.

For the slice FUNCAT experiments presented in **Figure 5C,D**, two regular-spiking CA1 interneurons located in *s. radiatum* were near-simultaneously patched using the K-based intracellular recording solution described above, supplemented with the morphological dye, Lucifer yellow (2 mM). One of the recording solutions also contained gelonin (3 μM) to block somatic protein synthesis. To enable *post-hoc* identification of the interneurons with confocal microscopy, contrast images of pipette position relative to slice orientation were collected. After the ~30 min loading period, during which cell health (e.g. holding current and membrane input resistance) were monitored electrophysiologically, the pipettes were carefully withdrawn such that the cell membrane could reform (which was confirmed in the confocal images, see below). Slices were then placed in carbogenated (95% O₂/5% CO₂) ACSF supplemented with 1 mM AHA for 2-3 hrs. After overnight fixation in 4% PFA and 5% sucrose PBS, slices were blocked and permeabilized in B-Block (10% donkey serum, 5% sucrose, 2% BSA, 0.1% Triton X) for 1 hr. Click-it® reaction was performed overnight with 1 μM Alexa Fluor-647 alkyne. Slices were imaged using confocal microscopy as described above. A z-stack spanning the entire soma of both cells was acquired. For analysis, two ROIs were selected

from the somatic cytoplasm (non-nucleus) and averaged to give a single value for each cell. Slices that did not contain both somata were excluded. Gelonin containing cells were identified by registering the confocal and contrast images.

Reverse transcription-polymerase chain reaction (RT-PCR)

Following the manufacturer's (Fermentas) instructions, isolated RNA was treated with DNase for 30 min at 37°C and then heat inactivated for 10 min at 65°C. cDNA reactions were prepared using Maxima RT with random hexamers (100 pM). Taq polymerase was used for subsequent PCRs with gene-specific primers for Arc (forward: GCT CGG TGA AGA ACT GGG TGG A; reverse: GGC TGG GTC CTG TCA CTG GCT A) and BDNF exon III (forward: CCC AGT CTC TGC CTA GAT CAA ATG G; reverse: ACT CGC ACG CCT TCA GTG AGA A). Band intensity quantified in ImageJ.

Gelonin/Alexafluor-488 protein labeling

Gelonin (~30 kDa) was incubated with reactive Alexa Fluor-488 (ThermoFisher Scientific) for 45 min, according to the manufacturer's instructions. Gelonin-488 containing solution was purified using a P6 Bio-Gel size exclusion chromatography resin column (BioRad). All eluted fractions (~1 mL each) were retained, and using a UV illuminator, fluorescence was identified in fractions 2, 6, 7, 8, and 9. To identify protein, 1 µL from each fraction was dotted on a nitrocellulose membrane and stained with Ponceau S (Sigma). Only fraction 2 was positive for protein. Gelonin-488 concentration was estimated from the known gelonin concentration added to the column and the total volume of each elution fraction. Just prior to experimentation, gelonin-488 was diluted into K⁺-based intracellular recording solution. The recording pipette tips were first front-filled with recording solution lacking gelonin-488 and then back-filled with solution containing gelonin-488. Estimated final concentration of gelonin-488 was ~3-30 µM. The morphological dye and M7 proxy Alexa Fluor-594 also was included in the recording solution. Interneurons in *s. radiatum* were whole-cell patch clamped and subsequently imaged using two-photon fluorescence microscopy (see below).

Two-photon microscopy

To track the diffusion of morphological dyes and M7 proxies (i.e. Alexa Fluor-594 and Lucifer yellow) and gelonin-488 in interneuron somata, dendrites, and putative axons, we carried out live imaging of loaded neurons in acute 400 µm thick slices using an Ultima In Vitro (Bruker Corporation) two-photon laser scanning fluorescence microscope (60x fluor objective, NA = 1.00, Nikon) equipped with an Insight Ti:Sapphire laser (Spectra Physics) tuned to 820 nm and a galvanometer-based scanhead. Laser power at the back aperture was between 5.6 and 31.7 mW. High intensity laser power was needed to detect signal in putative axons. To optimize dual color epifluorescence detection of Alexa Fluor-594 and Alexa Fluor-488, a 575 nm dxr dichroic mirror and 607/45 nm and 525/70 nm barrier filters were placed in front of the 'red' photomultiplier tube (PMT, multi-alkali, Hamamatsu) and 'green' PMT (GaAsP, Hamamatsu), respectively. Images were created on the NI 6110 board acquired with Prairie View 5.3U2 Beta software. During imaging, slices were constantly perfused with carbogenated ACSF at 25.0 ± 0.1°C. Z-stacks were collected shortly after achieving the whole-cell recording configuration and at various times (up to 1.5 hr) after loading Alexa Fluor-594 (250 µM), Lucifer yellow (250 µM), or gelonin-488 (3-30 µM). We loaded these concentrations to match the M7 and gelonin paired-recordings. Because gelonin-488 was expected to produce less fluorescence (detected with the green PMT) than Alexa Fluor-594, in an effort to detect gelonin-488 we set the green PMT gain higher than the red PMT gain. ImageJ was used for analysis. z-stacks were max projected. An ROI was selected from the corner of each channel (same location between channels), where there was no signal (i.e. background noise), and the mean gray value was computed. This value was respectively subtracted from each channel (i.e. red, green). Three circular ROIs were then selected from the soma, proximal dendrite, putative axon, and corners. The mean gray value was calculated for each. Values plotted are normalized to the soma for each fluorophore. For image presentation, z-stacks were max-intensity projected and background subtracted.

To assess microtubule integrity, we live imaged microtubule assemblies in 400 µm thick acute hippocampal slices using second harmonic generation microscopy (Barnes et al., 2010; Dombeck et al., 2003) on an inverted Olympus IX81 Fluoview FV1000 multiphoton microscope (25x XL plan N objective, NA = 1.05) equipped with a Mai Tai-Deep See Ti:Sapphire laser (Spectra Physics) tuned to 840 nm. The forward propagating second harmonic generation was collected in the transmitted direction, bandpass filtered at 425/30 nm (Semrock), and detected using a PMT (Hamamatsu). Images were acquired with Fluoview software. During imaging, slices were constantly perfused with carbogenated ACSF and maintained at 27.0 ± 0.1°C. Z-stacks were collected from mossy fibers in *s. lucidum*. Nocodazole was bath applied immediately after collecting the first z-stack (time 0). Images were collected at time 0 and 60 min later. Microscope settings remained constant during image acquisition. ImageJ was used for analysis. Circular ROIs were randomly selected from *s. lucidum* and analyzed at time 0 and 60 min. Data were normalized to the mean gray value for each group at time 0. For image presentation, z-stacks were max-intensity projected and background subtracted.

Stochastic optical reconstruction microscopy (STORM)

Experimental procedures were approved by the Hungarian Committee of the Scientific Ethics of Animal Research (License: XIV-1-001/2332-4/2012) and performed according to the Hungarian Act of Animal Care and Experimentation

(1998, XXVIII, Section 243/1998), which adhere to the European Council Directive of 1986 (86/609/EEC; Section 243/1998). Male Sprague-Dawley rats (P25, $n = 2$) and C57BL/6N mice (P27-41, $n = 11$) were deeply anesthetized, and acute hippocampal slices (300 μm thick) prepared as described (Lee et al., 2015). Slices recovered in solution containing (in mM): 75 sucrose, 85 NaCl, 2.5 KCl, 25 glucose, 1.25 NaH_2PO_4 , 4 MgCl_2 , 0.5 CaCl_2 , and 24 NaHCO_3 for 1 hr at 34°C and were then transferred to a chamber containing ACSF (in mM): 126 NaCl, 2.5 KCl, 26 NaHCO_3 , 2 CaCl_2 , 2 MgCl_2 , 1.25 NaH_2PO_4 , and 10 glucose, bubbled with 95% O_2 and 5% CO_2 for 60 mins at RT. The sections were transferred into PB (0.01 M phosphate buffer, $\text{pH} = 7.4$) containing 4% (wt/vol) PFA and fixed for 40 hrs at 4°C .

Tissue processing, immunostaining, and imaging were performed following our recently published protocol (Barna et al., 2016). Hippocampal slices were re-sectioned to 20 μm free-floating sections, washed extensively in PB and Tris-buffered saline (TBS, 0.05 M Tris and 0.9% (wt/vol) NaCl, $\text{pH} = 7.4$), and blocked in TBS containing 1% (wt/vol) BSA and 0.3% (vol/vol) Triton X-100. Sections were then incubated in TBS containing a combination of 2 or 3 (where indicated) of the following primary antibodies for 20 hrs at RT: affinity-purified guinea pig anti- CB_1 at 1:2000 (Fukudome et al., 2004); mouse monoclonal anti-5.8S rRNA, clone Y10b at 1:500 (Santa Cruz, sc-33678) (Lerner et al., 1981); rabbit monoclonal anti-rpS6, clone 5G10 at 1:200 (Cell Signaling, 2217); affinity-purified goat anti-parvalbumin at 1:5000 (Swant, PVG-214); mouse monoclonal anti-bassoon, clone SAP7F407 at 1:2000 (Abcam, ab82958); affinity-purified rabbit anti-bassoon at 1:1000 (Millipore, ABN255). After washing in TBS, sections were incubated in TBS containing a combination of 2 or 3 secondary antibodies (2 $\mu\text{g}/\text{mL}$) for 4 hours at RT: CF568 anti-guinea pig IgG (Biotium, 20377); CF568 anti-mouse (Biotium, 20105); Alexa Fluor-647 anti-mouse IgG (Jackson, 715-605-150); Alexa Fluor-647 anti-rabbit (Jackson, 711-605-152), Alexa Fluor-488 anti-goat (Jackson, 705-545-147); Alexa Fluor-488 anti-guinea pig (Jackson, 706-545-148); Cy3-Alexa Fluor-647 anti rabbit (prepared in-house). Sections were then washed in TBS and PB and mounted on glass coverslips.

To validate 5.8S rRNA-immunostaining specificity, we treated slices with nucleases. After fixation, sections were extensively washed in PB and incubated in TBS containing 0.3% (vol/vol) Triton-X100 for 30 mins. Sections were then washed 3x (10 mins each) in enzyme buffer (50 mM Tris and 5 mM CaCl_2 , $\text{pH} = 8$) and incubated for 60 mins at 37°C in enzyme buffer containing 300 U/mL micrococcal nuclease (New England Biolabs, M0247) and 30 $\mu\text{g}/\text{mL}$ RNase A (Fermentas, EN0531). For control experiments, nucleases were omitted from the buffer. After incubations, sections were extensively washed in PB and TBS and blocked for 45 mins in TBS containing 1% (wt/vol) BSA. Primary antibodies were added, and the immunostaining was completed as described above. For low-magnification images, samples were covered in Vectashield, and confocal images were recorded using a 20x plan apo VC objective (0.75 NA) on a Nikon AIR confocal microscope.

Correlated STORM and confocal imaging was carried out as described (Barna et al., 2016; Dudok et al., 2015). Samples were covered in imaging medium consisting of Dulbecco's PBS containing 5% (wt/vol) glucose, 0.1 M 2-Mercaptoethylamine (Sigma, 30070), 1 mg/mL glucose oxidase (Sigma, G2133), and 1500 U/mL catalase (Sigma, C30). Confocal z-stacks were collected using 488, 561, or 647 nm laser excitation and a Nikon CFI apochromat TIRF 100x oil immersion objective (1.49 NA) on a Nikon N-STORM setup equipped with a C2 confocal scan head. The same field of view was then imaged in astigmatic 3D directSTORM mode with continuous illumination through the TIRF unit (equipped with a 4x lens to focus the laser) with 405 nm and 647 nm laser excitation for 10,000 frames at 31 Hz for single-channel STORM. For dual-channel directSTORM (i.e. CB_1 and 5.8S rRNA), CF568 was selected for the second channel (Lehmann et al., 2016). Continuous illumination with either 405 nm and 561 nm or 405 nm and 647 nm laser was alternated every 2,500 frames for a total imaging length of 20,000 frames. For dual-channel STORM with sequential activation (i.e. 5.8S rRNA and rpS6), 8-frame cycles (activation with 405 nm and 561 nm, 3-3 frames of imaging with 647 nm after each activation frame) were repeated 1,500 times. After data acquisition, the confocal images were deconvolved with Huygens software (SVI). Identification of single-molecule localization points was performed with NIS-Elements N-STORM module (Nikon). Localization point precision was measured from the standard deviation of coordinates in isolated clusters (Dudok et al., 2015) at 13 nm and 34 nm in the lateral and axial dimensions, respectively. The numerically calculated localization accuracy for determining the position of one blinking event was 6.8 nm with single channel STORM and 10.6 nm with dual-channel STORM.

STORM and confocal image pairs were analyzed in VividSTORM. Axon terminal ROIs were selected using unbiased automated active contour selection. Preterminal axon segments were freehand selected. Nuclear ROIs (not including nucleoli) were selected with circles. Nanoscale spatial distribution of the STORM signal (i.e. localization points) was determined using custom-written scripts (Python). Clustering between localization points was assessed by determining the number of point pairs located within a series of 3D Euclidean search distances of a given ROI. This value was normalized to the mean of 100 randomized control measurements for each individual ROI. To quantify the distance of 5.8S rRNA localization points from the presynaptic plasma membrane, a 3D convex hull was fit to CB_1 localization points, clearly outlining the axon terminal. Somata and proximal dendrites were manually selected based on the 5.8S rRNA confocal image, and localization points within or outside these regions were categorized as cytosolic or neuropil, respectively. The distance (in 25 nm bins) of each 5.8S rRNA localization point inside and outside the terminal from the surface of the convex hull was calculated. Numbers of 3D localization points per bin were normalized to the area of the bin.

To estimate the relative quantity of ribosomal labeling in presynaptic compartments, images of CB₁ and PV confocal and 5.8S rRNA or rpS6 STORM immunostainings were segmented into 4 categories. Cell bodies and thick apical dendrites were selected manually based on the confocal image of ribosomal staining. CB₁ and PV channels were thresholded using Otsu's method, and positive pixels were used as the area for CB₁- and PV-positive processes, respectively. The uncategorized areas of the images contained ~25% of total STORM labeling. For the measurement of the distribution of ribosomal STORM signal in relation to the outline of the bouton and preterminal axon segment, a 2D spline was fit on the points of the ROI selection, and the 2D distance of each localization point from the spline was determined. For the distance from bassoon, the bassoon channel in the deconvolved confocal z-stack was thresholded, and the 3D position of positive voxels was recorded. The 3D distance of each localization point from the nearest bassoon-positive voxel inside the axon terminal was determined. To estimate the expected distributions, points (100 times the number of localization points) were placed in random 3D positions in each axon terminal, and the distances were measured as described above. Finally, the number of points per distance bin was normalized to the number of axon terminals (times 100 for randomized points). The 3D bouton views were generated using custom scripts. Perspective 3D STORM renderings of localization points were constructed using Visual Molecular Dynamics software. All images within each experiment were processed in parallel using identical imaging and analysis conditions.

Supplemental References

- Barna, L., Dudok, B., Miczan, V., Horvath, A., Laszlo, Z.I., and Katona, I. (2016). Correlated confocal and super-resolution imaging by VividSTORM. *Nature protocols* *11*, 163-183.
- Barnes, S.J., Opitz, T., Merckens, M., Kelly, T., von der Brélie, C., Krueppel, R., and Beck, H. (2010). Stable mossy fiber long-term potentiation requires calcium influx at the granule cell soma, protein synthesis, and microtubule-dependent axonal transport. *The Journal of neuroscience : the official journal of the Society for Neuroscience* *30*, 12996-13004.
- Chevaleyre, V., and Castillo, P.E. (2003). Heterosynaptic LTD of hippocampal GABAergic synapses: a novel role of endocannabinoids in regulating excitability. *Neuron* *38*, 461-472.
- Dombeck, D.A., Kasischke, K.A., Vishwasrao, H.D., Ingelsson, M., Hyman, B.T., and Webb, W.W. (2003). Uniform polarity microtubule assemblies imaged in native brain tissue by second-harmonic generation microscopy. *Proceedings of the National Academy of Sciences of the United States of America* *100*, 7081-7086.
- Dudok, B., Barna, L., Ledri, M., Szabo, S.I., Szabadits, E., Pinter, B., Woodhams, S.G., Henstridge, C.M., Balla, G.Y., Nyilas, R., *et al.* (2015). Cell-specific STORM super-resolution imaging reveals nanoscale organization of cannabinoid signaling. *Nature neuroscience* *18*, 75-86.
- Fukudome, Y., Ohno-Shosaku, T., Matsui, M., Omori, Y., Fukaya, M., Tsubokawa, H., Taketo, M.M., Watanabe, M., Manabe, T., and Kano, M. (2004). Two distinct classes of muscarinic action on hippocampal inhibitory synapses: M2-mediated direct suppression and M1/M3-mediated indirect suppression through endocannabinoid signalling. *The European journal of neuroscience* *19*, 2682-2692.
- Glickfeld, L.L., and Scanziani, M. (2006). Distinct timing in the activity of cannabinoid-sensitive and cannabinoid-insensitive basket cells. *Nature neuroscience* *9*, 807-815.
- Heifets, B.D., Chevaleyre, V., and Castillo, P.E. (2008). Interneuron activity controls endocannabinoid-mediated presynaptic plasticity through calcineurin. *Proceedings of the National Academy of Sciences of the United States of America* *105*, 10250-10255.
- Lee, S.H., Ledri, M., Toth, B., Marchionni, I., Henstridge, C.M., Dudok, B., Kenesei, K., Barna, L., Szabo, S.I., Renkecz, T., *et al.* (2015). Multiple Forms of Endocannabinoid and Endovanilloid Signaling Regulate the Tonic Control of GABA Release. *The Journal of neuroscience : the official journal of the Society for Neuroscience* *35*, 10039-10057.
- Lehmann, M., Lichtner, G., Klenz, H., and Schmoranz, J. (2016). Novel organic dyes for multicolor localization-based super-resolution microscopy. *Journal of biophotonics* *9*, 161-170.
- Lerner, E.A., Lerner, M.R., Janeway, C.A., Jr., and Steitz, J.A. (1981). Monoclonal antibodies to nucleic acid-containing cellular constituents: probes for molecular biology and autoimmune disease. *Proceedings of the National Academy of Sciences of the United States of America* *78*, 2737-2741.
- Pawelzik, H., Hughes, D.I., and Thomson, A.M. (2002). Physiological and morphological diversity of immunocytochemically defined parvalbumin- and cholecystokinin-positive interneurons in CA1 of the adult rat hippocampus. *The Journal of comparative neurology* *443*, 346-367.
- Rao, V.R., Pintchovski, S.A., Chin, J., Peebles, C.L., Mitra, S., and Finkbeiner, S. (2006). AMPA receptors regulate transcription of the plasticity-related immediate-early gene *Arc*. *Nature neuroscience* *9*, 887-895.
- Tao, X., Finkbeiner, S., Arnold, D.B., Shaywitz, A.J., and Greenberg, M.E. (1998). Ca²⁺ influx regulates BDNF transcription by a CREB family transcription factor-dependent mechanism. *Neuron* *20*, 709-726.
- Tom Dieck, S., Muller, A., Nehring, A., Hinz, F.I., Bartnik, I., Schuman, E.M., and Dieterich, D.C. (2012). Metabolic labeling with noncanonical amino acids and visualization by chemoselective fluorescent tagging. *Current protocols in cell biology / editorial board, Juan S Bonifacino [et al]* *Chapter 7*, Unit7 11.
- Younts, T.J., Chevaleyre, V., and Castillo, P.E. (2013). CA1 pyramidal cell theta-burst firing triggers endocannabinoid-mediated long-term depression at both somatic and dendritic inhibitory synapses. *The Journal of neuroscience : the official journal of the Society for Neuroscience* *33*, 13743-13757.